Journal of Non-Crystalline Solids 625 (2024) 122762

Contents lists available at ScienceDirect

Journal of Non-Crystalline Solids

journal homepage: www.elsevier.com/locate/jnoncrysol

Roots seeking of multiple shear-bands in amorphous alloys at the atomic scale

Huwen Ma [a,b], Haizhuan Song [a], Yuanfei Feng [a], Zhi Lyu [a], Li Feng [a,b,*], Tao Wen [e], Wangchun Duan [c,**], Peter K. Liaw [d,**], Yanchun Zhao [a,b,*]

[a] State Key Laboratory of Advanced Processing and Recycling of Non-Ferrous Metals, Lanzhou University of Technology, Lanzhou 730050, PR China
[b] Wenzhou Pump and Valve Engineering Research Institute, Lanzhou University of Technology, Wenzhou 325105, PR China
[c] Lanzhou Resources & Environment Voc-Tech University, Lanzhou 730123, PR China
[d] Department of Materials Science and Engineering, The University of Tennessee, Knoxville, TN 37996-2200, USA
[e] Gansu Computing Center, Lanzhou 730099, PR China

ARTICLE INFO

Keywords:
Amorphous alloy
Shear bands distribution
Molecular dynamics
Mechanical properties

ABSTRACT

The propagation of shear-bands is of utmost importance in understanding the macro and microscopic deformations of bulk metallic glasses (BMGs). In this study, using molecular dynamics simulations to elucidate the intricate atomic-scale mechanisms governing dynamic continuum shear-bands and microstructural evolution during deformation. This work provides compelling evidence of self-organized critical behavior, as evidenced by the observation of serrated flow patterns and distributions of elastic energy density. Moreover, we unveil the influence of notch length on the principal shear-band based on the steep stress drop (i.e., $\Delta\tau = \tau_y - \tau_s$, distinct from serrated flows), strength-normalized difference (i.e., $\Delta\tau/\tau_y$), and probability distribution of shear-strain. The effective blocking of shear bands by nanocrystal second phase can be attributed to the synergistic reinforcement effect of dislocations and nano-stacking faults. Finally, the analysis of the serrated flow behavior and stress-increment distribution during nanoindentation establishes the connection between micromechanical behavior, shear-band evolution, and macroscopic mechanical properties.

1. Introduction

Amorphous alloys possess a distinctive microstructure characterized by a short-range ordered and long-range disordered arrangement, devoid of common defects such as grain boundaries, dislocations, and stacking faults. These unique structural characteristics grant bulk amorphous alloys exceptional mechanical properties, including high strength, corrosion resistance, and wear resistance [1–4]. However, the limited tensile plastic deformation and failure of these alloys, primarily attributed to the rapid propagation of shear bands, impede their potential for widespread engineering applications [1,5]. Observing and tracking shear bands using surface and diffraction measurements present significant challenges, let alone studying their atomic-scale behavior.

Molecular dynamics calculations have emerged as one of the most effective approaches for investigating atomic-scale shear band propagation and microscopic-mechanical property variations. The OVITO analysis software is utilized to extract the motion path, arrangement, and comprehensive structural information of each atom in the system [6]. The formation of amorphous alloys generally involves extremely cold processing conditions, followed by the characterization of disorder and atomic arrangement using radial distribution functions (RDF), Honeycutt-Anderson bond angles, and bond-type analysis [7,8]. Falk et al. [9] employed molecular dynamics simulations to demonstrate the behavior of shear transformation zones (STZs) during deformation of amorphous alloys. They proposed a dynamical model for shear band deformation at low temperatures and determined the local strain of neighboring atoms using the least-squares method. Building upon this foundation, extensive research has been conducted on shear band evolution during the deformation of bulk metallic glasses (BMGs). By monitoring local atomic shear strain, the evolution of shear bands can be classified into three states: (1) below 4 % strain, an elastic state and

* Corresponding authors at: State Key Laboratory of Advanced Processing and Recycling of Non-Ferrous Metals, Lanzhou University of Technology, Lanzhou 730050, PR China.
** Corresponding authors.
E-mail addresses: fenglils@lut.edu.cn (L. Feng), 937041435@qq.com (W. Duan), pliaw@utk.edu (P.K. Liaw), zhaoyanchun@lut.edu.cn (Y. Zhao).

https://doi.org/10.1016/j.jnoncrysol.2023.122762
Received 7 September 2023; Received in revised form 28 November 2023; Accepted 29 November 2023
Available online 5 December 2023

homogeneous deformation with STZ initiation; (2) above 6 % strain, inhomogeneous deformation; (3) the critical shear strain required for shear band formation is 10 % [10]. The influence of loading conditions on the mechanical properties and behavior of STZs in amorphous alloys has garnered significant interest. For instance, Jiang et al. [11] discovered that increasing temperature weakens the mechanical properties while promoting STZ activation. Other researchers have explored the geometric factors of amorphous alloys, such as the presence of notches and multilayer amorphous structures. Yang et al. [12] studied the mechanical behavior of CuZr-based amorphous alloys with internal notches of varying sizes. Increasing the depth of the notch enhanced notch reinforcement and transformed the deformation mode from shear band spreading to mixed mode. Hua et al. [13] developed a nanoscale multilayer model of amorphous alloys with different compositions, $Cu_{80}Zr_{20}$ for layer A and $Cu_{20}Zr_{80}$ for layer B, and conducted molecular dynamics investigations of frictional-wear properties. The A/B and B/A layers exhibited contrasting frictional force trends with increasing grinding-ball depth, shedding light on the deformation mechanism of heterogeneous cross-sections during nano-scratch processes. To gain further insight into the limited ductility of amorphous alloys, several nanoscales second phases were introduced into the model. Song et al. [14] examined the mechanical properties of a nanometer-layered material composed of alternating amorphous and crystalline layers. They found that, for a fixed crystalline layer thickness, the yield strength increased as the amorphous layer thickness decreased, consistent with the Hall-Petch relationship, and that deformation behavior was governed by shear banding. In the 2010s, the transformation-induced plasticity (TRIP) effect was introduced into amorphous alloys to enhance their ductility. Subsequent molecular dynamics studies have shown remarkable growth in this field [15–19]. Wang et al. [19] investigated the influence of uniformly distributed spherical B2 phase on the mechanical properties of CuZr-based amorphous composites. Their findings revealed the activation of multiple shear bands due to the property mismatch between the B2 phase and the amorphous phase, and demonstrated the inhibitory effect of the B2 phase on the main shear band. In summary, the research focus of molecular dynamics studies on amorphous alloys has expanded from studying loading conditions and structural factors to encompass the influence of crystalline second phases in both stable and metastable states. However, these studies have predominantly focused on macroscopic properties, with limited attention paid to the nucleation and propagation of shear bands, which cannot be quantitatively analyzed solely based on shear band morphology.

Based on the aforementioned challenges, the serrated-flow phenomenon elucidates the initiation and propagation of shear bands at the microscale [20]. Zhu et al. [21] conducted a study on the $Cu_{55.7}Zr_{22.4}Ni_{7.2}Al_{4.7}$ amorphous alloy to investigate the influence of compressive strain rate on its plastic deformability and serrated-flow behavior. The serrated flow behavior was found to exhibit two distinct stages. In the first stage, the uniformity of the serrated flow is independent of the strain rate, whereas in the second stage, the flow transitions from a uniform to an inhomogeneous state due to shear band interactions. Nanoindentation serves as an effective technique for examining the serrated-flow behavior in amorphous alloys. Liao et al. [22] explored the impact of loading rates on the occurrence of serrated flow using nanoindentation. The results demonstrated that lower strain rates tend to trigger more pronounced serrations, whereas higher strain rates promote larger stress increments or abrupt stress drops in the serrated flow. These observations can be attributed to the development of a liquid-like region within metallic glasses. The increments in strain and stress during each serration signify the nucleation and growth of one or multiple shear bands, as well as their interactions [23,24]. Furthermore, researchers have discovered that the serrated flow not only manifests shear bands but also elucidates self-organized critical behavior [25]. This behavior can be exemplified by the sand pile model, in which sand accumulates when its inclination is below a critical threshold and collapses once it surpasses that threshold—a phenomenon known as self-organized critical behavior [26]. In amorphous alloys, the threshold corresponds to large-scale avalanches, specifically the spreading of main shear bands. Critical states preceding the occurrence of these avalanches typically arise at high strain rates, resulting from the interaction between the elastic strain fields of existing and newly-formed shear bands, which involves a substantial number of shear bands [27]. Enhancing the ductility of amorphous alloys can be achieved by delaying the onset of this threshold.

Additionally, the crystalline second phase is known to play a crucial role in reinforcing amorphous alloys. For instance, Wang et al. [28] demonstrated the ductility-enhancing effect of a crystalline Ni foam on BMGs through numerical calculation studies, showing significant dependence on the volume fraction. Liu et al. [29] successfully adjusted the size and homogenization of crystal particles by varying the Ta element content. They also showed that the crystalline second phase effectively blocked shear band and crack propagation, leading to excellent tensile properties. Ma et al. [30] revealed that the morphology and propagation of shear bands depended on the strength, lattice type, and volume fraction of the second phase. While previous research has focused on the shear-band evolution around the second phase, little attention has been given to the behavior of the crystal phase under shear forces without severe deformation. Recently, a method has been proposed to effectively overcome the strength-ductility trade-off by preparing nanoscale crystalline and amorphous composite materials. For instance, Ming et al. [31] fabricated a three-dimensional bicontinuous crystalline-amorphous nanostructure (3D-BCAN) with micron-sized equiaxed grains in a TiZr-based alloy using techniques such as melt spinning, copper mold suction casting, and arc melting. *In-situ* tensile and compressive experiments showed that BCANs exhibited superior uniform elongation (~7.0 %), tensile strength (~2.3 GPa), and yield strength (~1.8 GPa) compared to the amorphous and crystalline phases. This behavior was attributed to the additional strain hardening imposed by the amorphous phase on the crystalline phase, as well as the early suppression of shear band propagation in the amorphous phase by the crystalline phase. Wu et al. [32] fabricated a dual-phase material composed of a nano-crystalline core embedded in an amorphous matrix, where Mg was incorporated onto the amorphous matrix, via magnetron sputtering. This material exhibited a strength close to 3.3 GPa.

The aim of this study is to investigate the deformation behavior of amorphous alloys under different conditions. Molecular-dynamics simulations are employed to examine the effects of various factors, including loading rate, temperature, notch-geometry parameters, nanosecond phase size, and nano indenter size, on $Cu_{50}Zr_{50}$ amorphous alloys prepared by the extreme cold method. The mechanical behavior of amorphous alloys under different loading conditions is analyzed by varying the tensile strain rate and loading temperature, specifically focusing on serrated flow and self-organized critical behavior. Additionally, models of amorphous alloys with single-sided notches of different geometrical parameters have been prepared to study the influence of these factors on shear-band evolution and mechanical properties. Various analysis techniques, such as shear-strain-distribution plots, stress-strain curves, and shear-strain-probability distribution plots, are utilized. The introduction of a nanoscale second phase is also investigated, both in terms of percolation within the amorphous matrix and its synergistic resistance to shear deformation in conjunction with dislocations and nano-stacking faults. Furthermore, the behavior of shear bands and serrated flow during nanoindentation of amorphous alloys is examined, and the relationship with shear-band evolution is established through an analysis of stress increment distributions. This provides a link between macroscopic mechanical properties, shear bands, and microscopic mechanical behavior.

2. Simulation methods

Molecular dynamics simulations were conducted using the Lammps

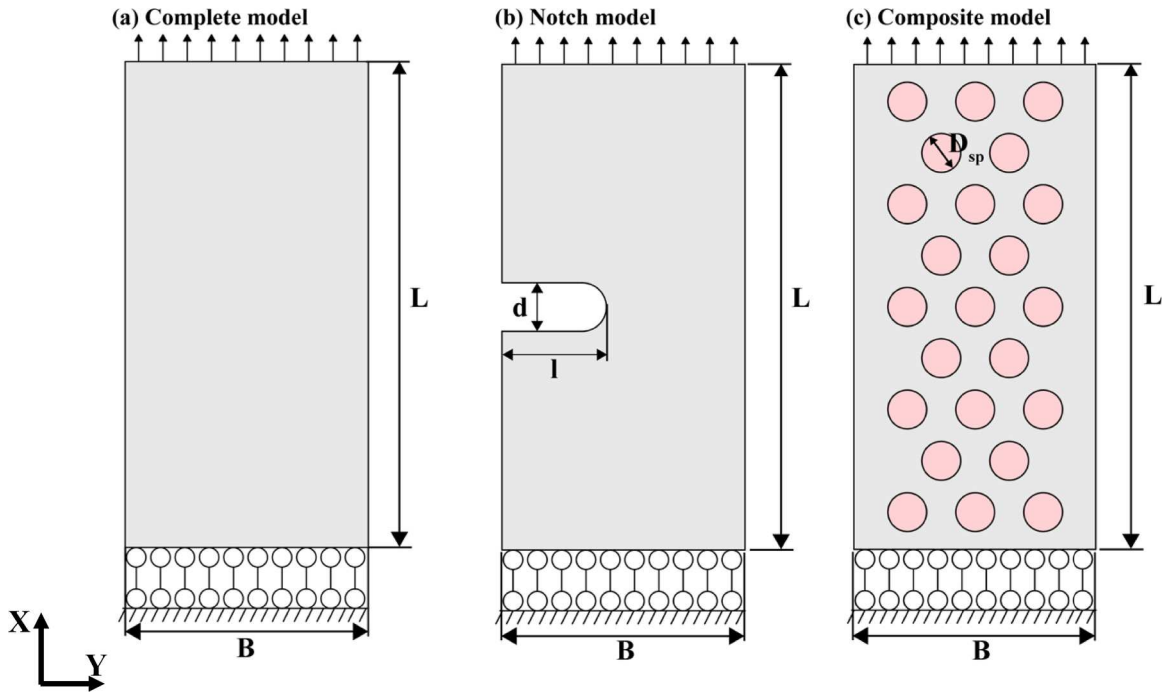

Fig. 1. Schematic diagram of the amorphous-alloy model used in molecular-dynamics simulations. Where the gray area shows the amorphous matrix phase, and the pink area represents the second phase. The dimensions of each model are different, as detailed in Section 2. (a) The pure amorphous-alloy model; (b) Notched model, where the notch length and width can be adjusted; (c) BMG-composite model with the adjusted volume fraction by changing the diameter of the nano-second phase.

software with the embedded atomic method (EAM) [33,34]. Nanoscale models of pure amorphous alloys, notched amorphous alloys, and amorphous composites containing a pure copper second phase were prepared, as shown in Fig. 1. The effects of temperature, strain rate, notch geometry, and second phase size on the mechanical behavior and shear-band evolution of amorphous alloys were investigated. The temperature and strain rate variation models consisted of 34,816 atoms in a plate model with dimensions of 28 nm × 13 nm × 1.6 nm. The notched and nanoindentation models consisted of 83,200 atoms (measuring 43 nm × 21 nm × 1.6 nm) and 770,560 atoms (measuring 71.3 nm × 465.5 nm × 4.1 nm), respectively. The modeling process was carried out as follows:

(1) Modeling of the amorphous alloy: Atomsk software was used to arrange 83,200 copper and zirconium atoms according to the B2 phase structure, creating a plate model measuring 42 nm × 20 nm × 1.5 nm. The model was set with periodic boundaries in the x, y, and z directions, with zero pressure, and a time step of 0.002 ps. Firstly, the energy was minimized using the conjugate gradient method [35], followed by a relaxation period of 200 ps at a temperature of 2100 K under constant-pressure, constant-temperature ensemble (NPT) conditions. This relaxed the system and allowed for uniform distribution of atoms. Subsequently, the model was cooled to 50 K at a rate of 2 K/ps, serving as the subsequent stretching temperature, which could be adjusted based on the specific model requirements. The amorphous alloy model with periodic boundary conditions was obtained by performing NPT relaxation for 200 ps at 50 K to bring the system to equilibrium. For velocity stretching, the boundary conditions were changed to periodic in the x direction and systolic in the y and z directions using the change-box command. An additional 200 ps of NVT (canonical ensemble) relaxation was performed. Moreover, for nanoindentation simulations, the boundary conditions were changed to periodic in the x and y directions, and systolic in the z direction (p s), followed by 100 ps of NVT relaxation.

(2) Modeling of the notch, composites, and nanoindentation: The notch model involves deleting the atoms in the notch region. Afterward, it undergoes relaxation for 200 ps under NPT conditions until the system reaches equilibrium. To create the composite-material model, a 42 nm × 20 nm × 1.5 nm pure Cu-plate model is initially established. Then, the second phase is prepared by removing specific atoms. The corresponding vacancies are cut out on the amorphous plate model, and the second phase is spliced together with the parent phase. The combined model undergoes a 200 ps NPT relaxation to achieve equilibrium. For the nanoindentation models with a larger size, the direct preparation process is time-consuming due to the increased number of atoms. To address this, an amorphous model of the entire quarter size is built. Then, it is duplicated twice in the length and thickness directions. Finally, NPT relaxation is performed to achieve equilibrium.

(3) Uniaxial stretching and nanoindentation processes: The uniaxial stretching experiments involve employing velocity stretching to impose controlled deformation on the material. The upper and lower ends of the sample are fixed at a distance of 1 nm, and the stretching is performed under NVT (constant number of particles, volume, and temperature) conditions. By modifying the boundary condition to periodic in the x direction and systolic in the y and z directions, the velocity stretching method effectively reveals the development of shear bands within the material. A tensile rate of $0.8 \times 10^8\ s^{-1}$ is applied to both the notch and composite models to capture the material's deformation behavior. These models are tensile tested at a temperature of 50 K, allowing for enhanced characterization of the deformation response [36]. The nanoindentation experiments are carried out under controlled conditions, involving a temperature of 50 K and NVT relaxation. Semicircular indenters with diameters of 15 nm and 10 nm are employed to apply controlled indentation forces on the atoms. The force-displacement relationship is governed by the equation:

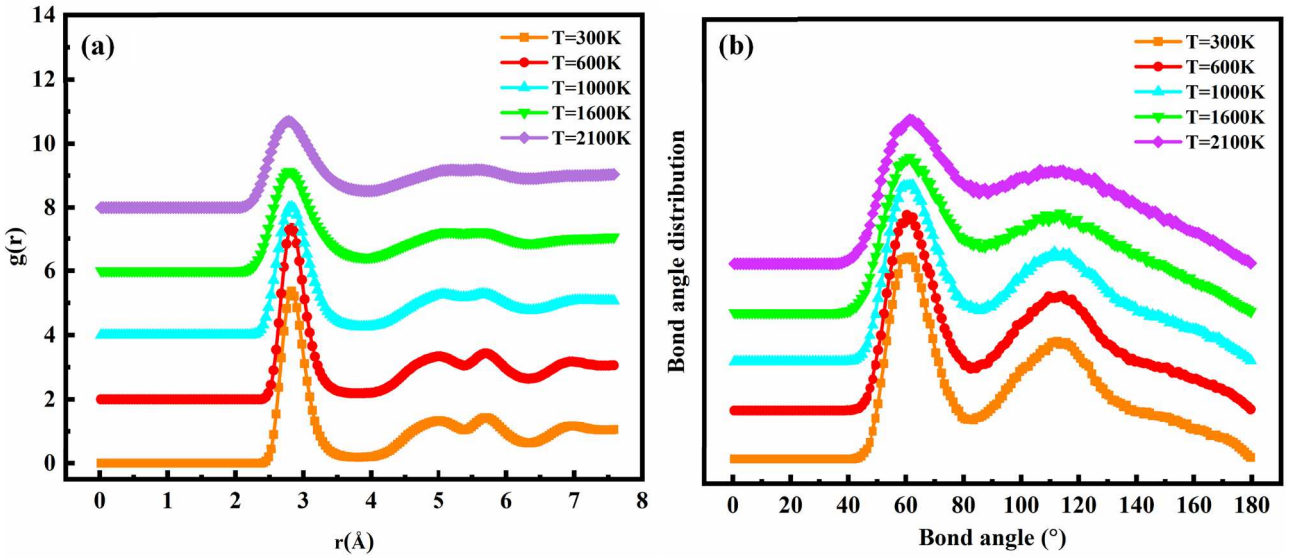

Fig. 2. Evolution of the atomic structure of CuZr alloys during the process from 2100 K extreme cold to 300 K. (a) The radial distribution function (RDF) during the cooling process of CuZr-based amorphous alloys; (b) The bond-angle distribution function during the cooling process of CuZr-based amorphous alloys.

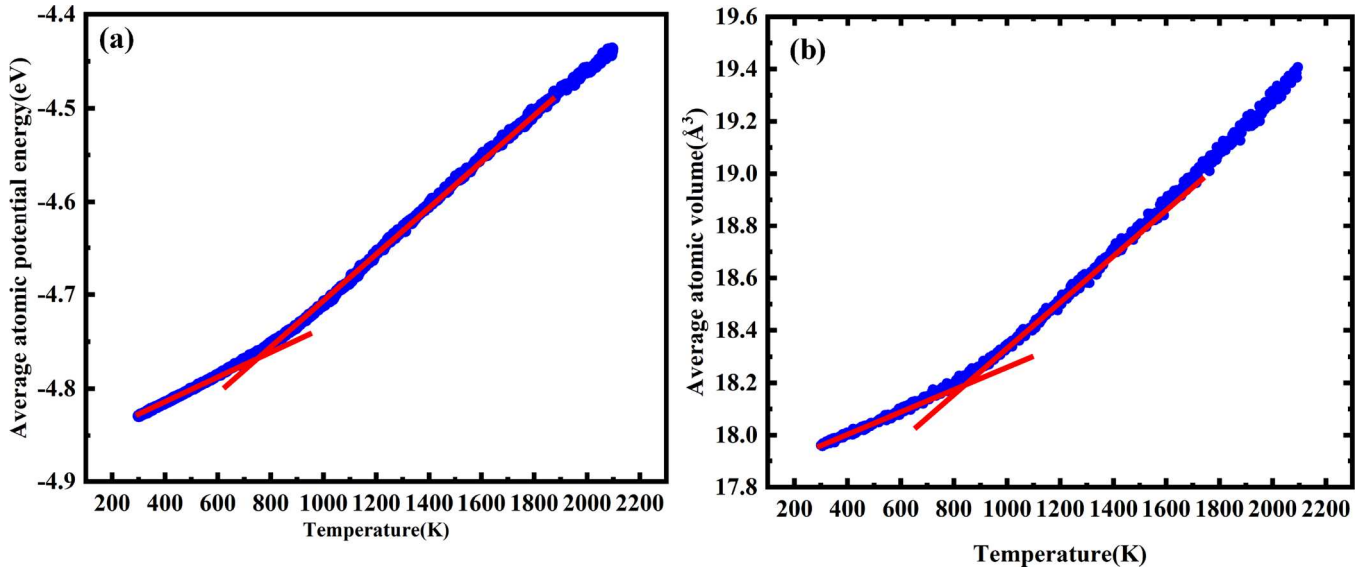

Fig. 3. Average atomic volume and atomic potential-energy curves for a $Cu_{50}Zr_{50}$ amorphous alloy with cooling from 2100 K to 300 K. Where the intersection of the tangent lines before and after the change in slope is the glass-transition temperature. (a) average atomic-potential energy; (b) average atomic volume.

$$F(r) = -K(r-R)^2 \quad (1)$$

Here, K represents the force constant, set to 3.3 eV/Å^3 in this study, r represents the radial distance from the atom to the axis of the indenter, and R denotes the radius of the indenter. The morphology of the resulting shear bands and any associated changes in the crystal structure are visualized and analyzed using the OVITO software, consistent with previous findings [37,38]. This study utilizes the Cu-Zr embedded atom method (EAM) potential developed by Mendelev [39], which is extensively employed in numerous amorphous simulations involving CuZr-based systems and demonstrates a consistent trend with experimental observations, thereby affirming the effectiveness of this approach and indicating a relatively small level of systematic errors [40–46]. To address random errors, key simulations are repeated twice.

3. Results and discussion

3.1. Structural study of amorphous alloys

The radial distribution function (RDF) analysis has proven to be an effective method for studying the structural characteristics of CuZr-based amorphous alloys. In Fig. 2(a), the RDF curve reveals distinct features of the alloy's structure in different phases, including crystalline, amorphous, and liquid states [47]. At a temperature of 300 K, the amorphous alloy exhibits a sharp and intense peak in the RDF, indicating a high degree of order in the nearest neighboring atoms. This is attributed to the low thermal agitation at lower temperatures and the strong retention of the liquid phase structure in the solid phase due to rapid cooling rates. The increased intensity and narrowing of the first peak suggest an increase in coordination number and enhanced orderliness of neighboring atoms. Observations of the RDF at 1000 K and lower temperatures reveal a noticeable splitting peak, which becomes

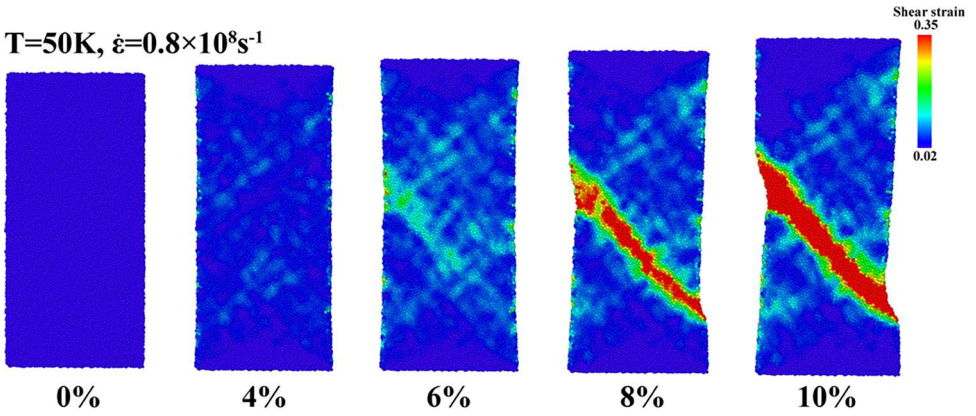

Fig. 4. The shear-strain-distribution plot of a $Cu_{50}Zr_{50}$ amorphous alloy with the temperature at 50 K and strain rate at 0.8 × $10^8 s^{-1}$. As the macroscopic strain increases, the shear strain is concentrated in one band, i.e., the main shear band.

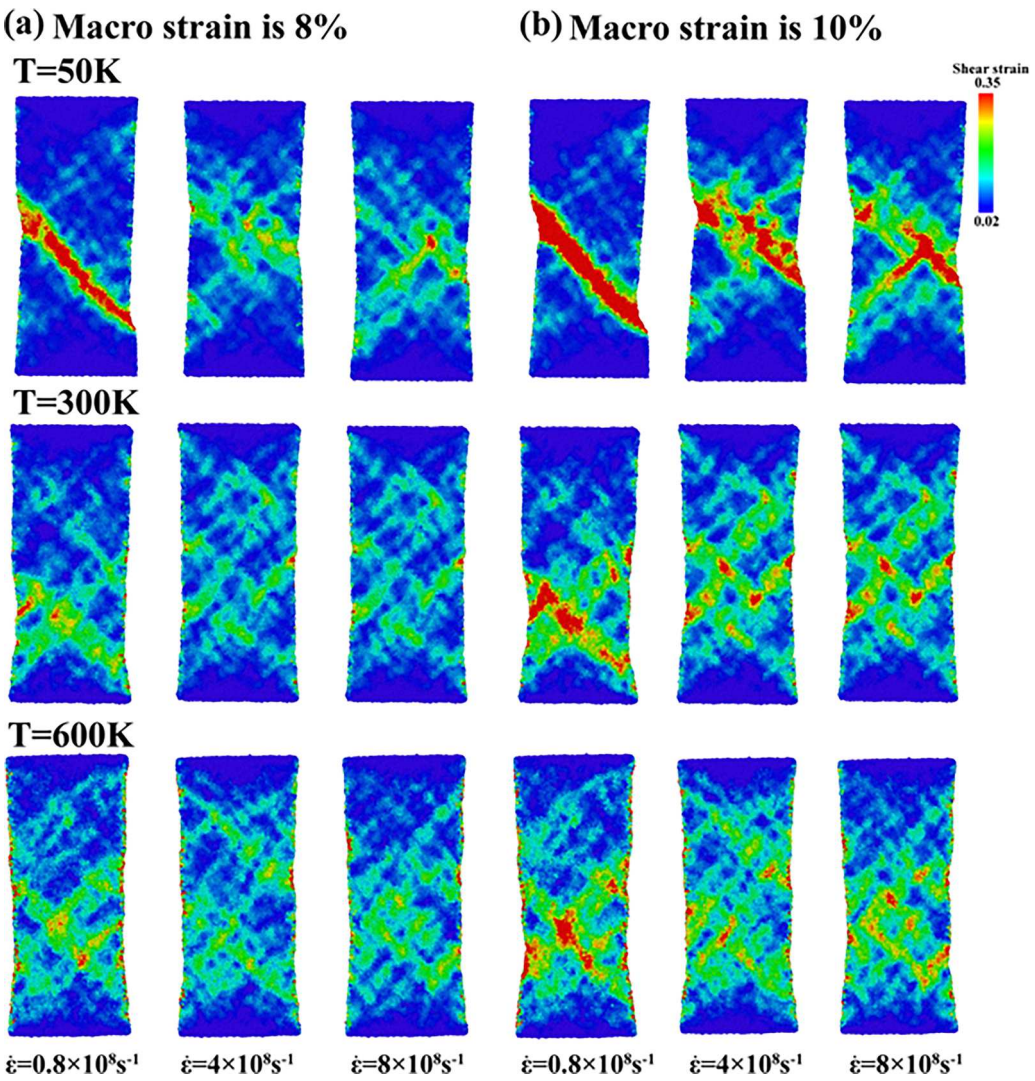

Fig. 5. Shear-strain plots of CuZr-based amorphous alloys at different temperatures and loading rates. (a) macroscopic strain at 8 %; (b) macroscopic strain at 10 %. The high temperature and strain rate induce multiple shear bands.

more pronounced as the temperature decreases. This splitting phenomenon is a characteristic feature during the formation of amorphous alloys [48]. The determination of the amorphous structure also relies on the analysis of the bond-angle distribution. Short-range ordered structures, such as icosahedral clusters, are indicative of amorphous alloys' atomic packing arrangements [49]. In the face-centered cubic structure, peaks are observed at angles of 60°, 90°, and 120°, while in the body-centered cubic structure, peaks appear at 70.5° and 109.5°.

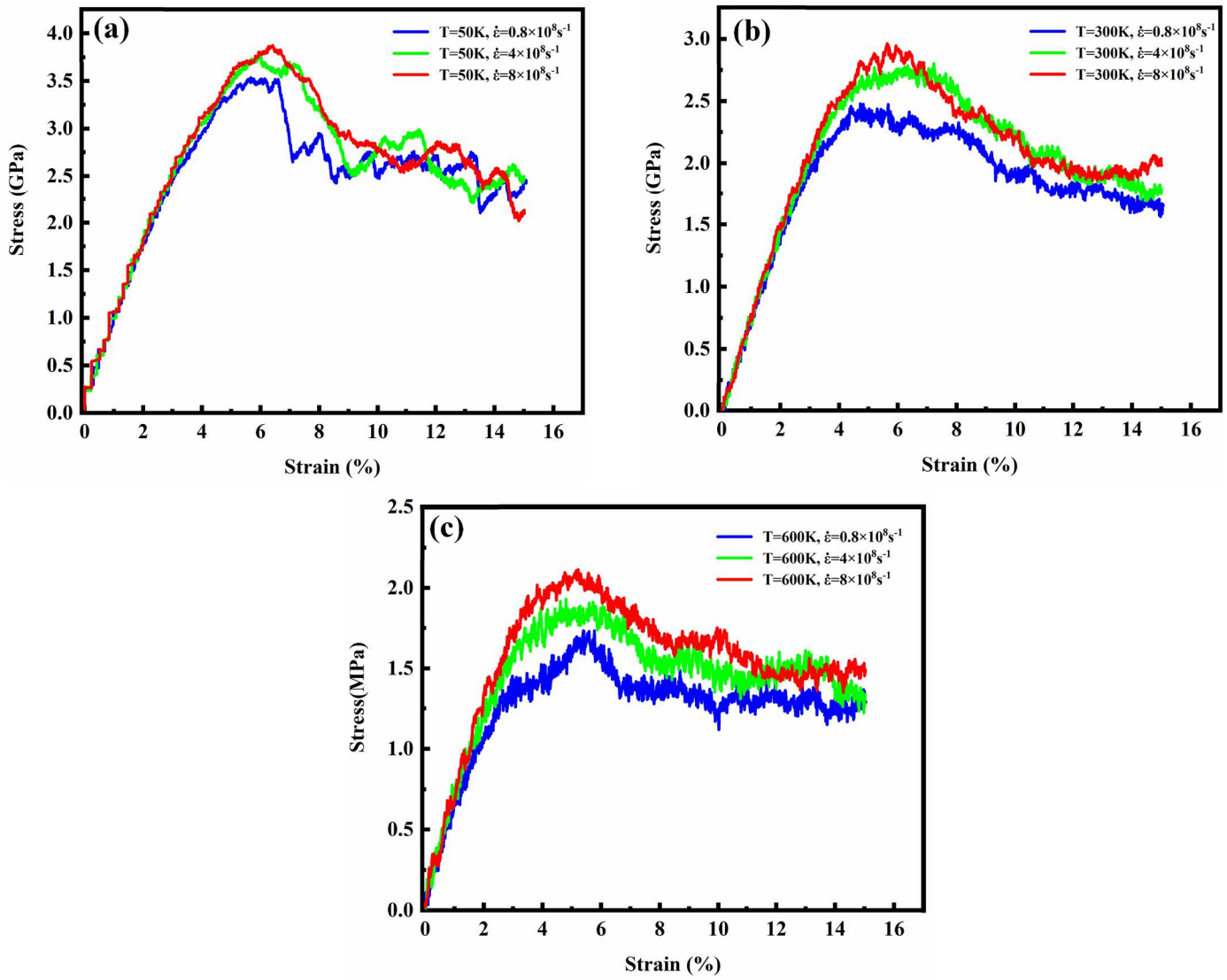

Fig. 6. The stress-strain curves of the $Cu_{50}Zr_{50}$ amorphous alloy at different temperatures and strain rates, which have a significant serrated flow behavior. (a) T = 50 K; (b) T = 300 K; (c) T = 600 K.

Icosahedral structures exhibit peaks at 63.4° and 116.6°. As seen in Fig. 2(b), the bond-angle distribution of the amorphous structure shows an increasing trend compared to the liquid-phase structure at room temperature, with the peaks approaching those of the standard icosahedron. The presence of shoulder peaks indicates a higher degree of order, suggesting a propensity for the formation of icosahedral structures during the transition from the extremely cold liquid phase to the solid phase [50].

In Fig. 3, the temperature-dependence curves depict the average atomic volume and the average atomic potential energy of CuZr-based amorphous alloys in the temperature range of 2100 K to 300 K. As the temperature decreases, the amplitude of thermal vibrations decreases, leading to a reduction in both the average atomic volume and potential energy. The process of crystallization is considered a primary phase transition, which often involves a change in volume. In contrast, the formation of the amorphous phase represents a secondary phase transition, characterized by a change in slope rather than a sudden change in volume. The transition from the liquid phase to the amorphous phase is indicated by a change in slope occurring at around 870 K, which corresponds to the glass-transition temperature. Therefore, the RDF, bond-angle distribution, and average atomic potential energy curves collectively validate the establishment of the CuZr-based amorphous alloy model.

3.2. *Mechanical properties of amorphous alloys at different temperatures and tensile rates*

In this section, tensile simulations were conducted on CuZr-based amorphous alloys at three different strain rates and temperatures. Specifically, three temperature levels of 50 K, 300 K, and 600 K were selected, along with three strain rate levels of 0.8 × 10^8s^{-1}, 4 × 10^8s^{-1}, and 8 × 10^8s^{-1} at each temperature. The shear-strain distribution diagrams for different temperatures and strain rates are shown in Figs. 4 and 5, demonstrating various degrees of shear-strain concentrations resulting from different loading conditions. The process of shear-band formation is exemplified at a temperature of 50 K and a strain rate of 0.8 × 10^8s^{-1}. As depicted in Fig. 4, a small amount of a Shear Transformation Zone (STZ) is observed on the surface of the amorphous alloy at low levels of macroscopic strain. With an increase in macroscopic strain to 6 %, the shear-transition zone exhibits the prototype of a shear band. As the macroscopic strain exceeds 8 %, the amorphous alloy undergoes significant deformation along a single main shear band. The process of shear-band expansion in amorphous alloys corresponds to the three stages of tensile deformation, with STZ being rarely formed in the

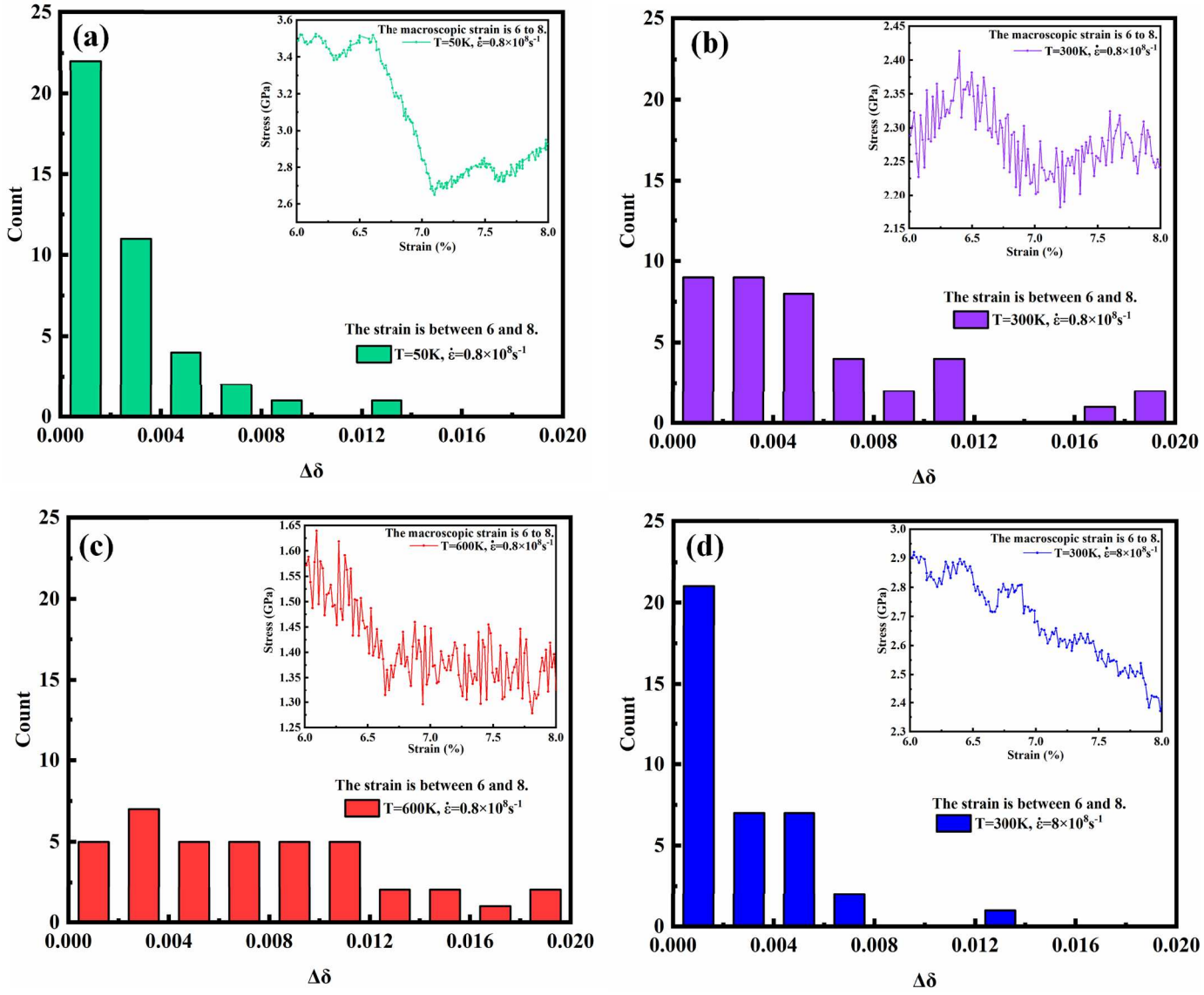

Fig. 7. The elastic-energy density of the $Cu_{50}Zr_{50}$ amorphous alloy at strains between 6% and 8% with different temperatures and strain rates is plotted statistically. (a) T = 50K, $\dot{\varepsilon}$= 0.8 × 10^8s^{-1}; (b) T = 300 K, $\dot{\varepsilon}$= 0.8 × 10^8s^{-1}; (c) T = 600 K, $\dot{\varepsilon}$= 0.8 × 10^8s^{-1}; (d) T = 300 K, $\dot{\varepsilon}$= 8 × 10^8s^{-1}.

elastic-deformation stage, the alloy relying mainly on STZ in the plastic deformation stage albeit for a short duration, and the failure stage being primarily attributed to the rapid propagation of shear bands [51].

The shear-strain distribution diagrams at macroscopic strains of 8 % and 10 % are shown in Fig. 5, allowing for a more detailed comparison of the shear-band evolution under different loading conditions. Analyzing the effects of various strain rates on the shear band evolution at a temperature of 50 K, it is evident that the concentration of Shear Transformation Zones (STZs) decreases with increasing strain rates, and the formation of the main shear band is delayed. Additionally, the impact of different temperatures on the shear band evolution at the same loading rate can be examined. The shear-strain distribution diagram reveals that as the temperature increases, the localization of STZs decreases, favoring the formation of multiple shear bands. The formation of shear bands in amorphous alloys is attributed to thermal fluctuations that provide sufficient energy for local atomic clusters to overcome the potential barrier for shear deformation. Therefore, the increase in temperature enhances the thermal vibration of atoms, facilitating STZ formation and leading to the occurrence of multiple shear bands [52]. As a result of more dispersed STZs, the strain generated during the tensile process may be more evenly distributed among multiple shear bands, resulting in a significant increase in the strain rate. The stress-strain curves for CuZr-based amorphous alloys at different temperatures and strain rates are depicted in Fig. 6. With an increase in the loading rate, the fracture strength of the amorphous alloy continuously increases, and the plastic deformation ability also exhibits an upward trend. This phenomenon can be explained by considering the distribution of shear bands mentioned earlier. The higher strain rate converts plastic work into heat in a short period, leading to a sudden increase in thermal vibration of the atoms and activating more STZs [53].

Moreover, the avalanche behavior of stress drop (associated with the formation of main shear bands, not the serrations) becomes more prominent at lower strain rates for amorphous alloys, as indicated by the blue line in Fig. 6(a). Comparing the stress-strain curves at different temperatures, CuZr-based amorphous alloys demonstrate higher yield strength, fracture strength, and elastic modulus, as well as more significant avalanche behavior at lower temperatures. This can be attributed to stronger atomic bonding at low temperatures and a lower degree of thermal activation, requiring higher external forces to induce shear band formation. Furthermore, the serrated flow behavior observed in the stress-strain curve indicates that higher temperatures correspond to higher vibration frequencies, with each vibration representing the

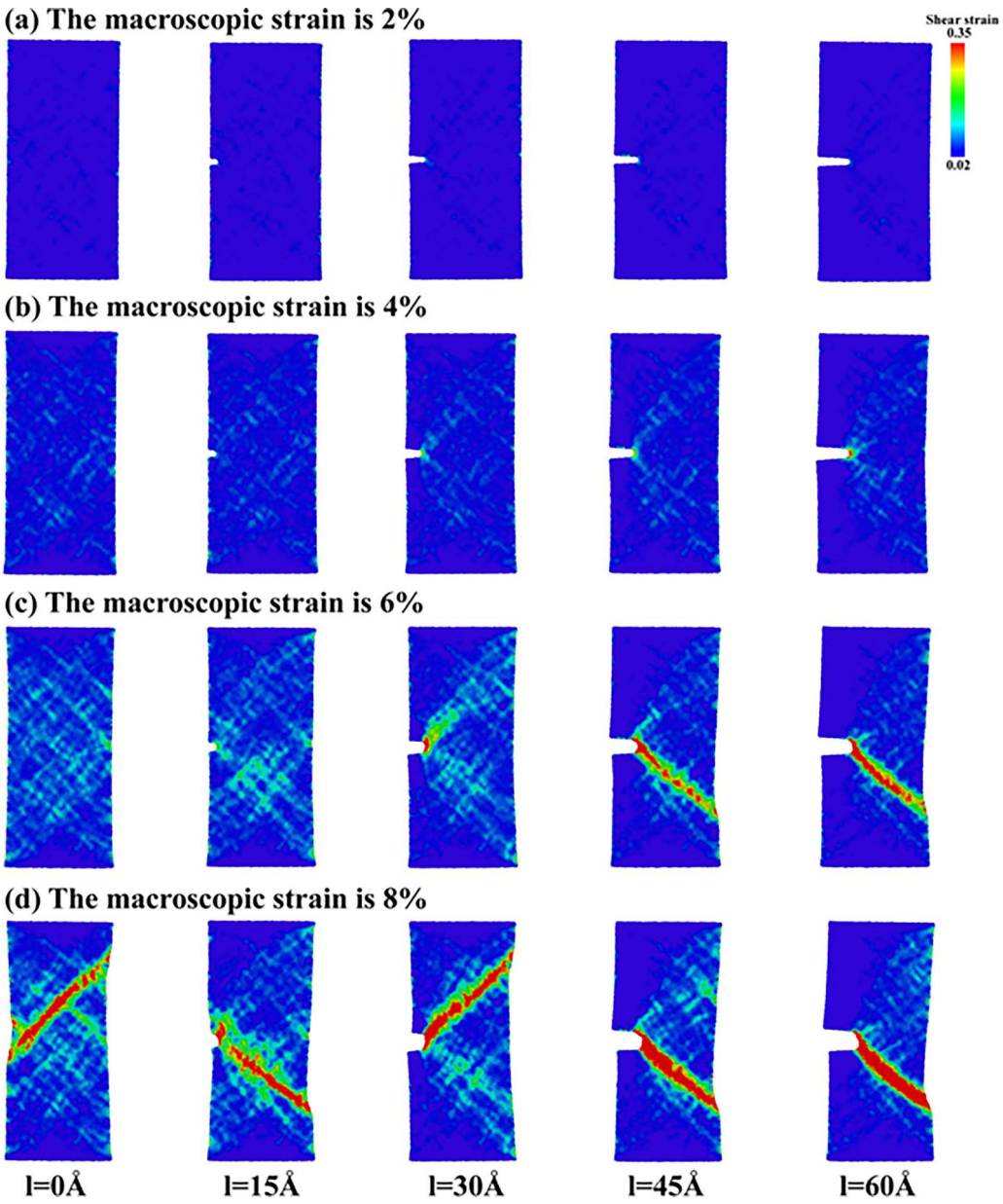

Fig. 8. Shear strain distribution plots of the $Cu_{50}Zr_{50}$ amorphous alloy at different notch lengths when the notch width is 10 Å. (a) macroscopic strain at 2 %; (b) macroscopic strain at 4 %; (c) macroscopic strain at 6 %; (d) macroscopic strain at 8 %.

nucleation of a shear band and the amplitude denoting the extent of shear band expansion [54,55].

To study the formation and propagation of shear bands, a segment of the pre-failure stress-strain curve was selected to examine the behavior of serrated flow. The stress-strain curves and corresponding statistical distribution of elastic energy density for the $Cu_{50}Zr_{50}$ amorphous alloy were presented in Fig. 7, encompassing macroscopic strains ranging from 6 % to 8 % under different temperatures and strain rates. CuZr-based amorphous alloys exhibit significant elastoplastic deformation behavior, manifested by pronounced serrated flow after elastic deformation [56]. Upon comparing the magnified stress-strain curves, it is evident that the amplitude and frequency of the serrated flow behavior are greatly influenced by the temperature and strain rate during tensile deformation. Lower temperatures and higher strain rates result in reduced amplitude and frequency. As previously discussed, the frequency and amplitude of serrations serve as indicators of shear band formation and expansion, capturing the avalanche phenomenon involving shear band coalescence and release of elastic energy. To quantitatively investigate the critical self-organization behavior of shear bands, the elastic energy density of serrations is recorded using the following formula [25]:

$$\Delta\delta = \frac{1}{2}\Delta\sigma \times \Delta\varepsilon \tag{2}$$

Here, $\Delta\sigma$ represents the stress increment of the serration, and $\Delta\varepsilon$ represents the strain increment of the serration, as depicted in Fig. 16. At a temperature of 50 K, the elastic energy density is primarily distributed within the range of 0 to 0.004. With increasing temperature, more serrations with higher elastic energy density are formed. This implies that higher temperatures provide sufficient energy for the transition of atomic clusters to shear bands, facilitating their expansion. The presence of a significant number of serrations with low elastic energy density indicates that higher strain rates impede the prompt release of energy within the elastic strain field, promoting the occurrence of secondary shear bands [Fig. 7(d)]. The elastic strain field formed by both new and pre-existing shear bands facilitates the transition of the amorphous alloy

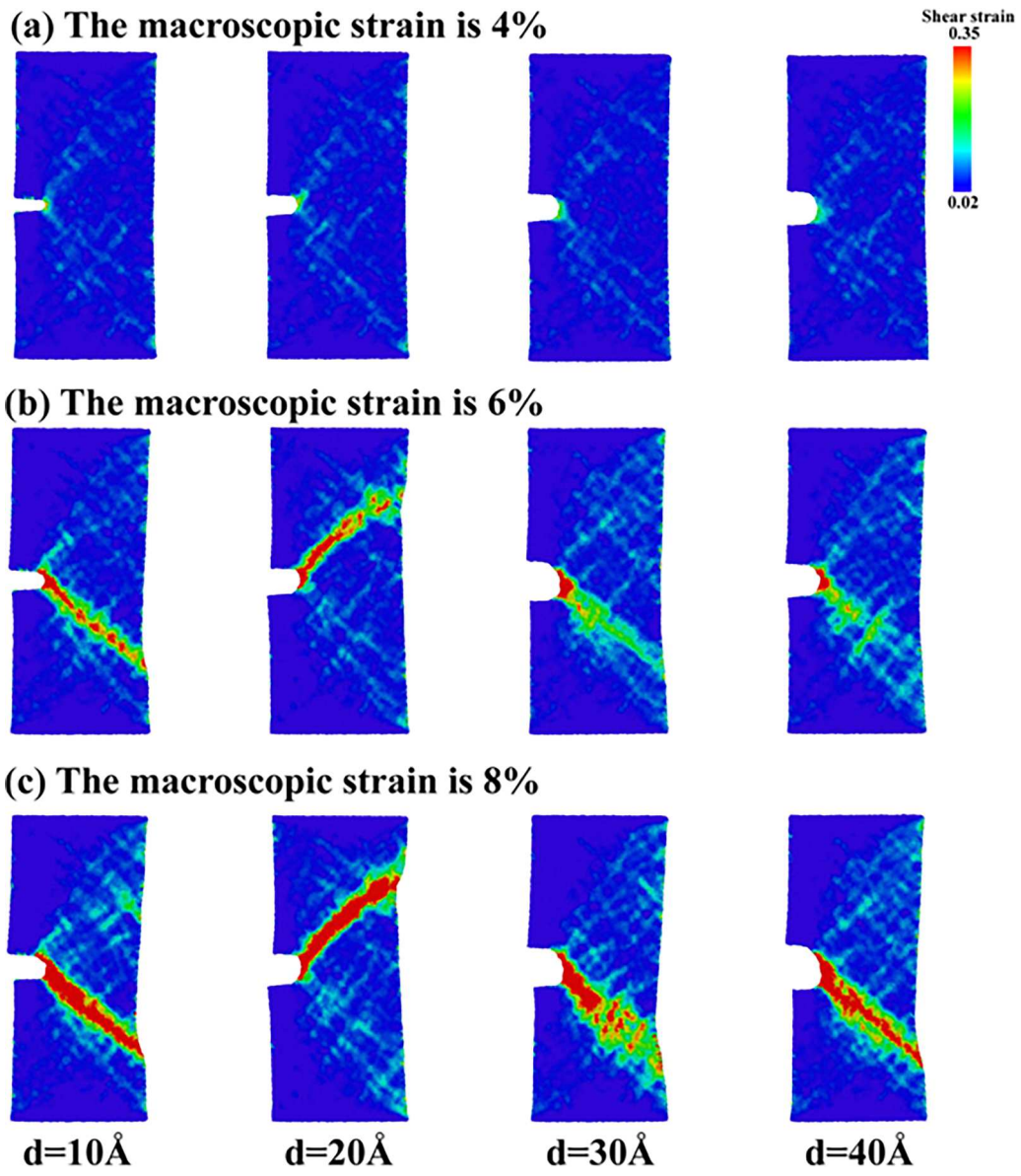

Fig. 9. Shear strain distribution plots for $Cu_{50}Zr_{50}$ amorphous alloy at different notch widths with the notch length is 45 Å. (a) macroscopic strain at 4 %; (b) macroscopic strain at 6 %; (c) macroscopic strain at 8 %.

from plastic dynamics to self-organized critical behavior [27]. According to Fig. 7(b) and (d), lower strain rates allow the elastic strain field to have sufficient time to release energy, thereby minimizing the interaction between shear bands, and the plastic deformation is in a chaotic state. In high-temperature deformation of amorphous alloys, the increase in thermal energy of atoms or molecules leads to enhanced amplitude and frequency of thermal vibrations, causing the evolution process of local structure, macroscopic deformation, and microscopic strain field in the amorphous alloy to become highly complex, thus resulting in chaotic states as shown in Fig. 7(a) and (c). Conversely, higher strain rates are not conducive to the full expansion of shear bands and may lead to the formation of more numerous small-scale shear bands. These results are consistent with previous studies [57].

3.3. Effect of notch size on the mechanical behavior and shear-band evolution of amorphous alloys

The mechanical behavior and shear-band evolution of the $Cu_{50}Zr_{50}$ amorphous alloy with unilateral notching during uniaxial stretching were simulated using molecular dynamics, establishing the connection between shear bands and mechanical properties. The shear-strain distribution diagrams of the CuZr-based amorphous alloy at different notch lengths were displayed in Fig. 8. Initially, at a macroscopic strain of 2 %, a small amount of shear transformation zones (STZ) is dispersed on the alloy's surface. Increasing the macroscopic strain results in concentrated STZ near the notch. With further loading strain, models with larger notch lengths form more complete single shear bands. When the macroscopic strain exceeds 8 %, all models have formed mature shear bands, with the maturity increasing with the notch length. This phenomenon can be attributed to notch-induced stress concentrations, which enhance atomic movement and facilitate crossing the potential energy barrier, leading to STZ formation. Additionally, at a macroscopic strain of 4 %, there is a tendency to form multiple shear bands due to the second-notch effect, where the plate sample transitions from a double-force corresponding state to a three-dimensional stress state [58,59]. However, the rapid nucleation and expansion of one shear band does not provide additional ductility benefit to the amorphous alloy. Furthermore, the effect of different notch widths on tensile plasticity and

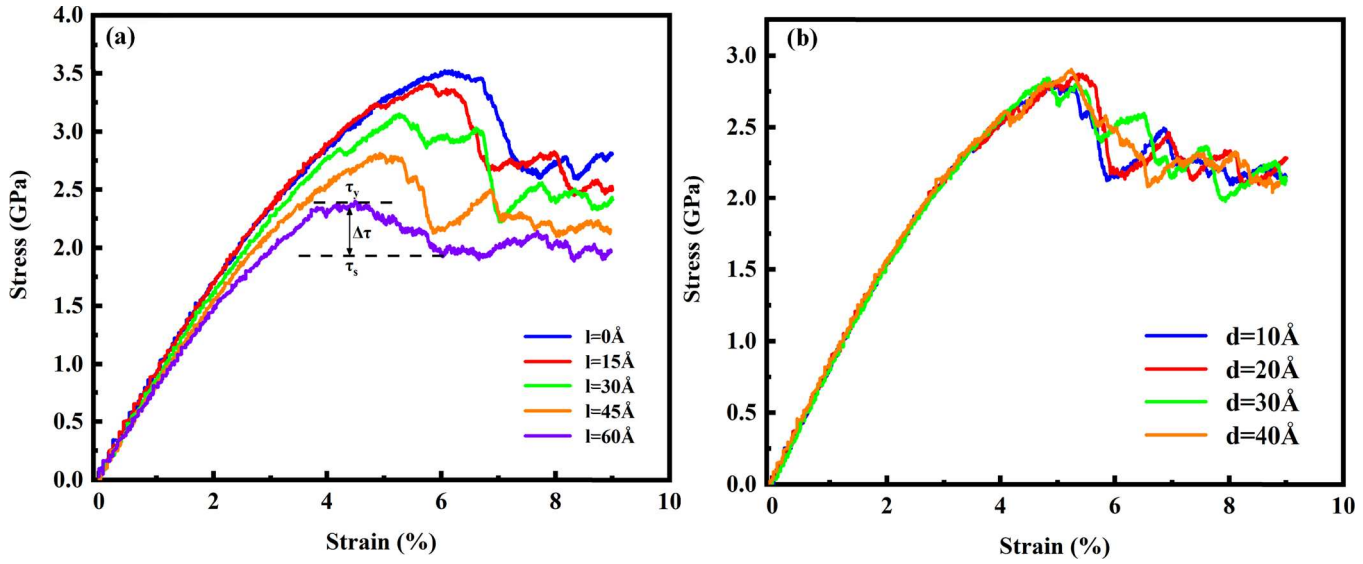

Fig. 10. The stress-strain curves of the $Cu_{50}Zr_{50}$ amorphous alloy at different notch sizes. (a) Variation of notch length; (b) Variation of notch width.

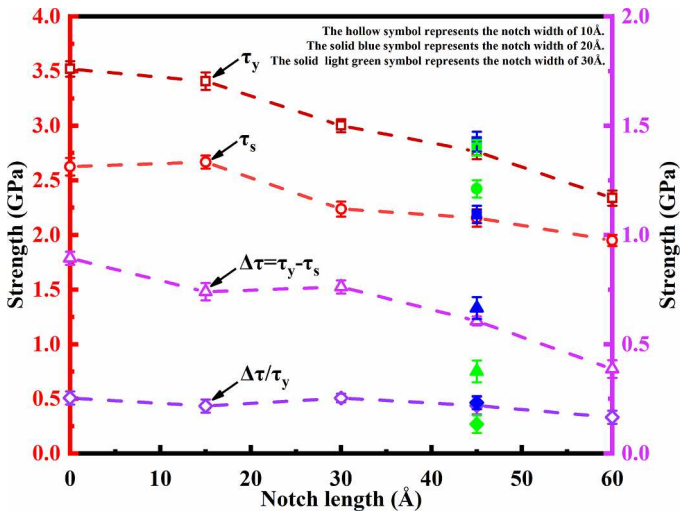

Fig. 11. The plots of yield strength (τ_y), relative steady-state strength (τ_s), steep stress drop values ($\Delta\tau = \tau_y - \tau_s$), and normalized difference in strength ($\Delta\tau/\tau_y$) for the $Cu_{50}Zr_{50}$ amorphous alloy at different notch sizes. The two red curves correspond to the left ordinate and the two purple curves correspond to the right ordinate.

shear-band morphology was investigated by fixing the notch length at 45 Å, as presented in Fig. 9. The formation of shear bands can be effectively delayed when the notch width reaches 30 Å. This trend can be attributed to the larger width inducing more shear bands under the three-dimensional stress state and delaying the formation of a single main shear band.

Fig. 10 displays the stress-strain curves of the $Cu_{50}Zr_{50}$ amorphous alloy with different notch sizes. The stress-strain curves provide insights into the distribution of shear bands, with larger notches leading to earlier onset of avalanche behavior. The steep stress-drop value ($\Delta\tau = \tau_y - \tau_s$, distinguishing it from the weak stress drop in serrated flow), yield strength (τ_y), and relative steady-state strength (τ_s) decrease. Here, τ_y represents the stress required for plastic deformation, while τ_s denotes the strength of shear band spreading in amorphous alloys [60]. The decrease in stress drop is attributed to the increased notch length and decreased shear band extension length. Furthermore, the maximum shear strain values of each model at a macroscopic strain of 6 % were extracted, which were 0.32, 0.34, 0.79, 1.30, and 1.56, respectively, indicating the influence of notch length on shear band nucleation and propagation. Study on notch widths shows that increasing width does not significantly reduce the tensile strength. However, widths greater than 30 Å weaken the avalanche effect, which corresponds to the synergistic deformation behavior of multiple shear bands. It is important to note that the simulated tensile strengths are higher than the actual tensile strength due to several factors: (1) The tensile strain rate used in the simulations is higher than the actual rate, as the actual rate would exceed the capability of molecular dynamics calculations. (2) A temperature of 50 K was used in this work to prevent issues related to atomic motion caused by temperature fields [60]. (3) The simulations were conducted under ideal conditions, disregarding defects, pores, and other factors.

As presented in Fig. 11, the yield strength, relative steady-state strength, stress drop and normalized difference of strength ($\Delta\tau/\tau_y$) all show a decreasing trend with the increase of notch length. Meanwhile, the increase of notch width makes $\Delta\tau$ and $\Delta\tau/\tau_y$ increase first and then decrease, where $\Delta\tau/\tau_y$ represents the trend of strain localization [61]. In the above phenomena, the slight decrease of a strain-localization trend caused by the increase of notch length may be due to the decrease of shear-band length, and the influence of width increase on the localization trend is consistent with the above analysis. Figs. 12 and 13 present the maximum shear strain diagram and shear strain probability distribution diagram, respectively, for the $Cu_{50}Zr_{50}$ amorphous alloy across varied notch sizes. Initially, an increase in notch length leads to a continuous rise in both the magnitude of shear strain and the probability of encountering larger shear strains, indicating an expanding shear band effect, as illustrated in Fig. 12(b)–(f). Subsequently, the maximum shear strain corresponding to different macroscopic strains was plotted in the maximum shear strain diagram, with a spline curve fitted to the dotted line in Fig. 12(a). The graph clearly depicts a consistent increase in the maximum shear strain value with the rise in macroscopic strain, while the increasing trend is exacerbated with greater notch length. This finding once again confirms the promotive role of notch length in the nucleation and growth of shear bands, while concurrently compromising the strength and plasticity of amorphous alloys. Observing Fig. 13, a subtle decrease in both high strain probability and maximum shear strain is observed with increasing notch width. This behavior can be ascribed to the formation of multiple shear bands, aligning with the analysis of shear band morphology and stress-strain curves.

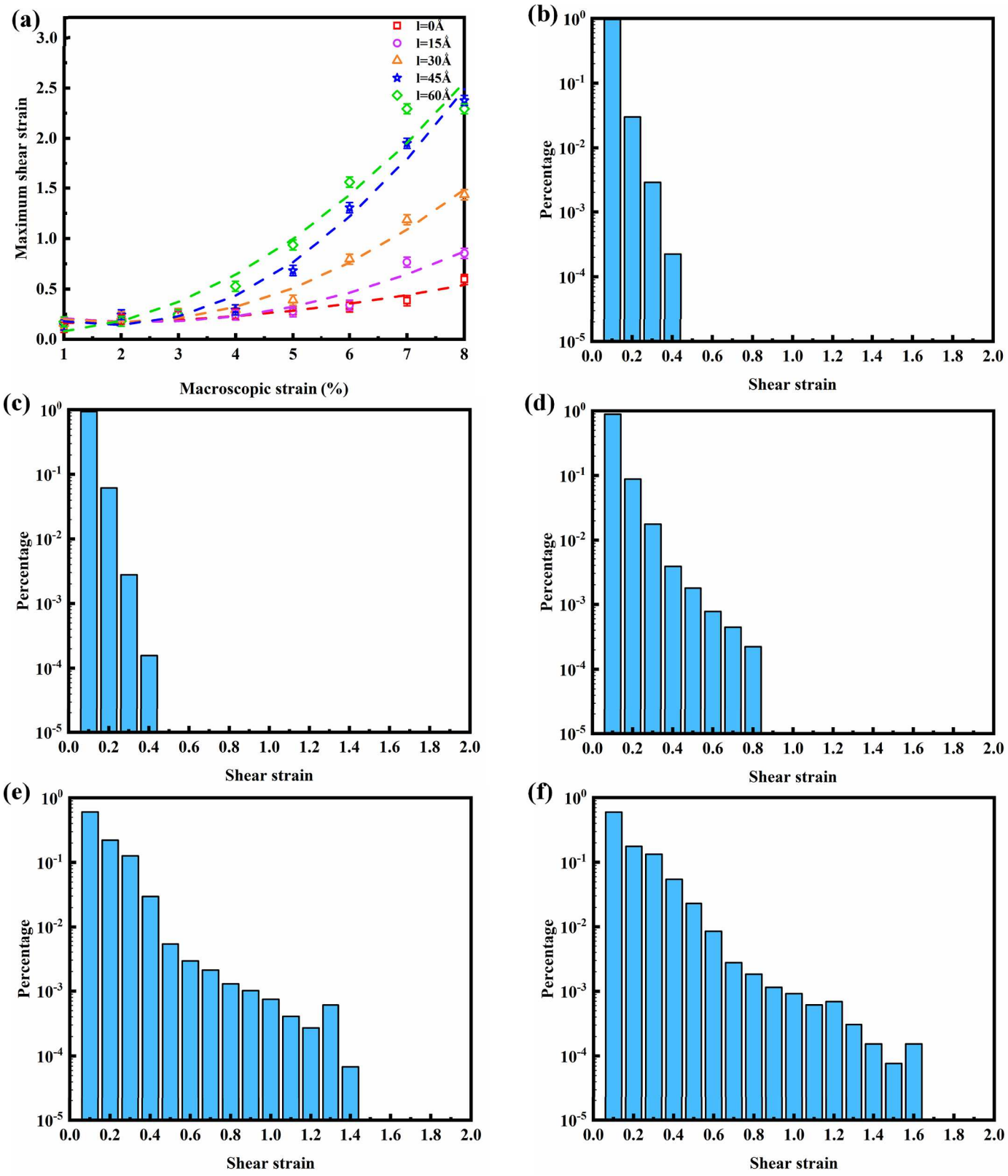

Fig. 12. Statistical plots for the maximum shear strain and probability charts of the shear strain at a macroscopic strain of 6 % at different notch lengths for the $Cu_{50}Zr_{50}$ amorphous alloy, ignoring the shear strain less than 0.02. (a) Plot of the maximum shear strain with increasing the macroscopic strain; The probability diagram of shear strains with notch lengths, including 0 Å (b), 15 Å (c), 30 Å (d), 45 Å (e), and 60 Å (f).

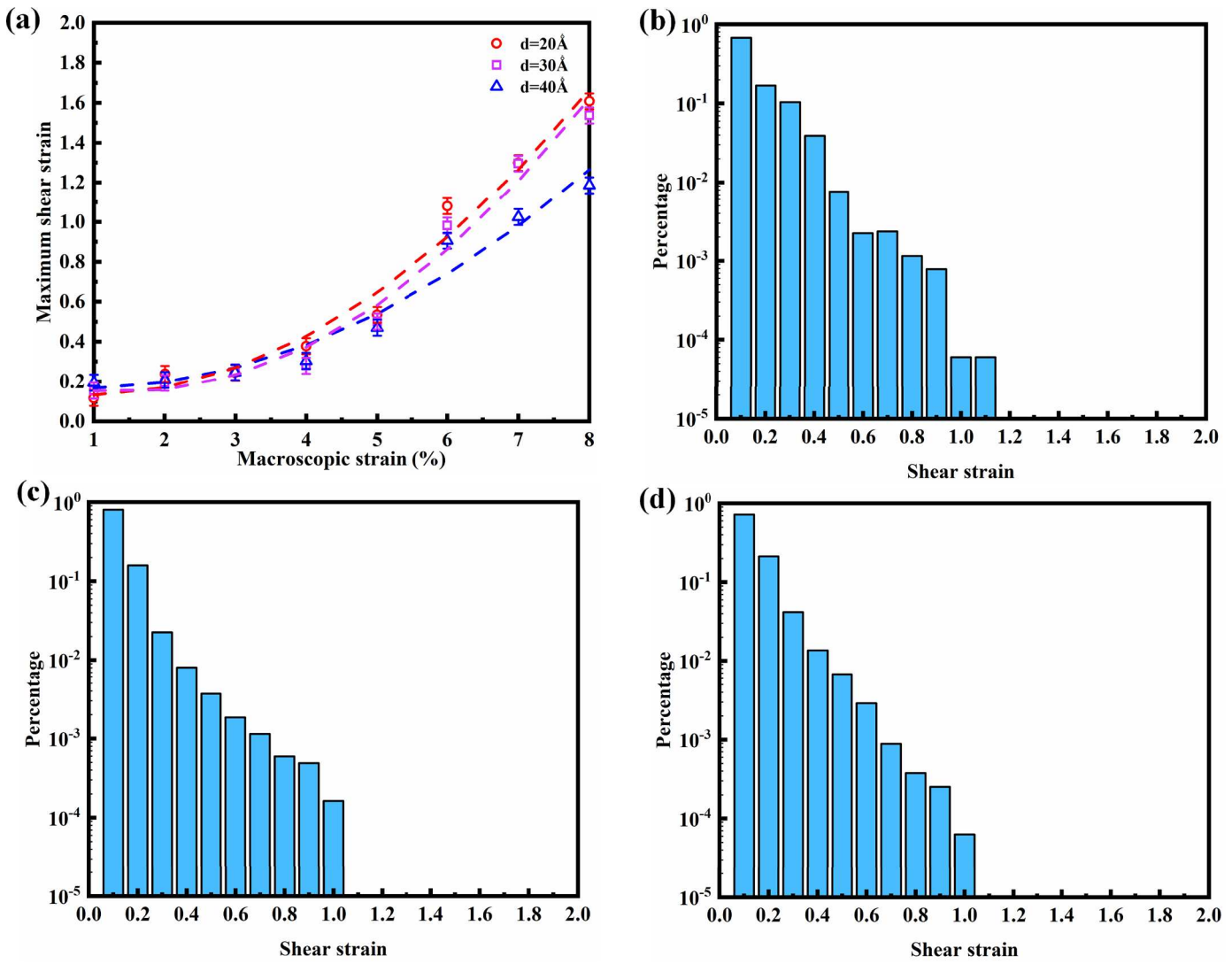

Fig. 13. Statistical plots for the maximum shear strain and probability charts of the shear strain at a macroscopic strain of 6 % at different notch widths for the $Cu_{50}Zr_{50}$ amorphous alloy, ignoring the shear strain less than 0.02. (a) Plot of the maximum shear strain with increasing the macroscopic strain; The probability diagram of shear strains with notch widths, including 20 Å (b), 30 Å (c), and 40 Å (d).

3.4. Nanoindentation behavior of amorphous alloys

This section aims to compare the impact of different indenter sizes and loading speeds on the distribution of shear bands in the amorphous alloy and analyze the correlation between serrated-flow behavior and shear band evolution. Fig. 14(a) and (b) portray the shear-strain cloud diagrams of the CuZr-based amorphous alloy under the same loading speed but with different indenter sizes. It can be observed that the indenter with a diameter of 10 nm exhibits a more pronounced effect on the initiation of shear bands in the early stage of the indentation process compared to larger indenters. This could be attributed to the smaller indenter resulting in the formation of a stress concentration area, where the stress field dominates the nucleation and expansion of shear bands. As a result, the shear bands form at a 45° angle with respect to the downward pressure direction and concentrate beneath the indenter [62]. Furthermore, the shear bands formed during nanoindentation take on an arched shape rather than a straight line. This phenomenon can be explained by the shear bands forming in response to alleviate the stress field effect. It is important to note that the formation of shear bands releases a significant amount of heat energy, which is rapidly dissipated by the amorphous parent phase. Localized heat treatment and atomic rearrangement might potentially induce crystallization within the shear bands, thereby impeding their expansion and enhancing ductility. However, no evidence of crystallization was found in this study [63,64]. When comparing the model with a loading speed of $v = 0.1$ Å/ps to the one with $v = 0.5$ Å/ps, it was observed that the former exhibits a higher density of shear bands. This phenomenon cannot be solely explained by the shear-strain cloud diagram and will be elaborated in more detail in the subsequent analysis of the serrated flow behavior.

Fig. 15 illustrates the displacement load curves of CuZr-based amorphous alloys, employing different indenter sizes and loading speeds. All three curves exhibit prominent serrated-flow behavior. In comparison to the $D_{indenter} = 15$ nm case, the smaller indenter exhibits higher frequency and amplitude of serrations during the initial loading stage. These frequency and amplitude variations correspond to the nucleation and expansion of shear bands, consistent with the shear-strain-cloud diagram's findings. Furthermore, a lower pressing speed induces a more pronounced serrated-flow behavior, as depicted in Fig. 15. Beyond a loading depth of 3 nm, there is a significant increase in both frequency and amplitude. This indicates that the nanoindenter's size and loading rate significantly influence the observed serrated-flow behavior.

Due to the presence of long-range disorder and short-range order microstructure, the plastic flow behavior of bulk metallic glasses is

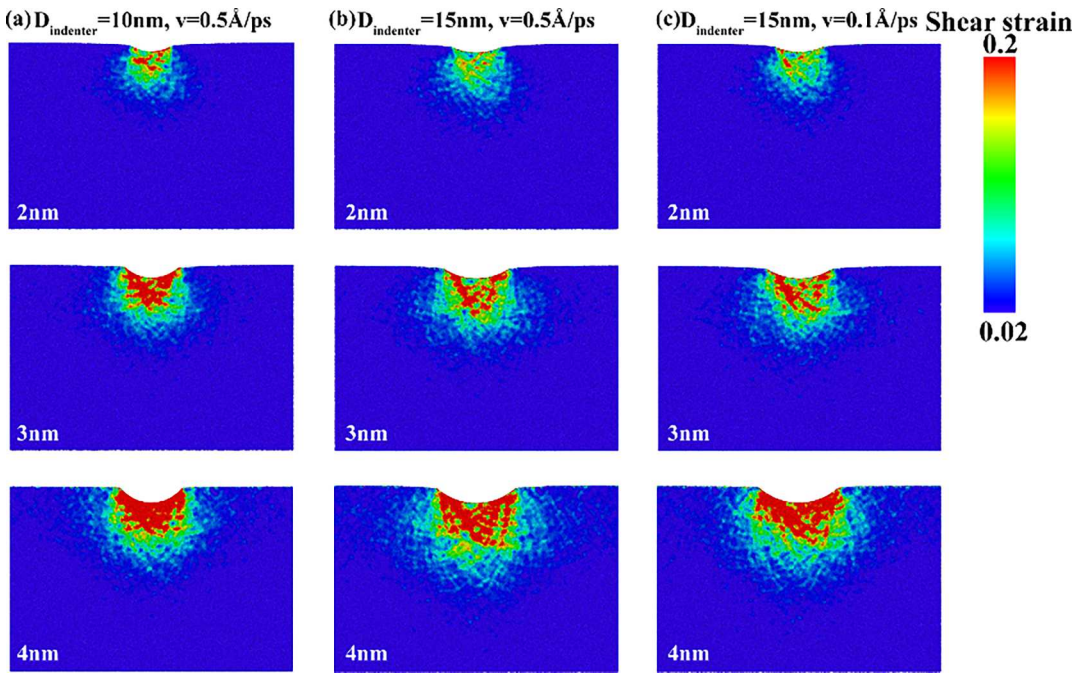

Fig. 14. Distribution of shear strain in the $Cu_{50}Zr_{50}$ amorphous alloy under different indenter sizes and pressing rates. (a) $D_{indenter}$ = 10 nm, v = 0.5 Å/ps; (b) $D_{indenter}$ = 15 nm, v = 0.5 Å/ps; and (c) $D_{indenter}$ = 15 nm, v = 0.1 Å/ps.

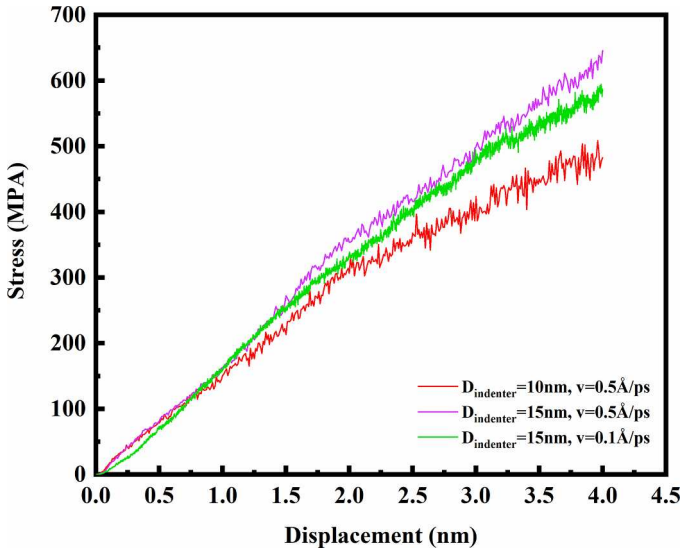

Fig. 15. Load-displacement curves of the Cu50Zr50 amorphous alloy with different indenter sizes and pressing rates.

predominantly governed by the displacement and propagation of shear bands. The magnitude of the stress drop observed during serrated flow reflects both the relaxation of elastic energy and the length of the shear band [65]. Fig. 16 presents the statistical distribution of stress increments plotted against the magnitude of stress increment for the serrated flow regime between displacements of 3.5 nm and 4.0 nm, as shown in Fig. 15. Comparing the case with a 10 nm diameter indenter to the Dindenter = 15 nm case, it is evident that the smaller indenter activates a larger stress increment, which is consistent with the findings from the shear-strain-cloud diagram. Huang et al. [66,67] reported that the formation of shear bands during nanoindentation experiments may not depend on the loading rate, but rather on the relative passivation of the Berkovich indenter. Similarly, in our study, the use of a larger diameter indenter induces a weaker stress field, resulting in a less pronounced sensitivity to the loading rate. Slower loading rates lead to the activation of more serrations, primarily concentrated in the stress range of 0 to 20 MPa. This suggests the formation of a greater number of shear bands, although their extent of propagation is relatively limited. These observations challenge the currently utilized shear-band propagation dynamic (SBPD) model, which assumes that the shear band propagation rate exceeds the indenter's loading rate, allowing for the production of serrated flow with significant stress increments [68]. The semi-circular indenter used in this study does not possess sharp corners, thereby lacking the ability to generate a strong enough elastic-strain field to induce large-scale shear avalanches within the amorphous matrix [20]. Instead, the elastic-strain field associated with the primary shear bands promotes the formation of secondary shear bands, ultimately leading to the occurrence of high-frequency serrated-flow behavior.

3.5. Role of a nanoscale second relative shear band

In recent years, there has been significant interest in investigating the nano-crystallization of amorphous alloys as a means to enhance their mechanical properties. In the study conducted by Fan et al. [69], Zr-based amorphous alloys with nanocrystalline grains were prepared using arc melting and vacuum casting techniques under an argon atmosphere. The results demonstrated that the strength and plasticity of the alloys increased with an increasing volume fraction of nanocrystalline grains, reaching maximum plasticity during the early stages of nano-crystallization. However, the underlying mechanisms responsible for the improvements in strength and ductility achieved by nanocrystalline grains have received limited attention. In this section, the introduction of a nano-scale Cu crystal phase into CuZr-based amorphous alloys through atom substitution was investigated to study the impediment it poses to shear bands and other strengthening effects during uniaxial tensile testing. The shear-strain cloud diagrams for the amorphous composites containing the nano-scale Cu crystal second phase are presented in Fig. 17. It can be observed that multiple shear bands are formed in all three amorphous composites, with an increasing trend of multiple shear bands as the size of the second phase increases. Moreover, an increase in the size of the second phase effectively reduces

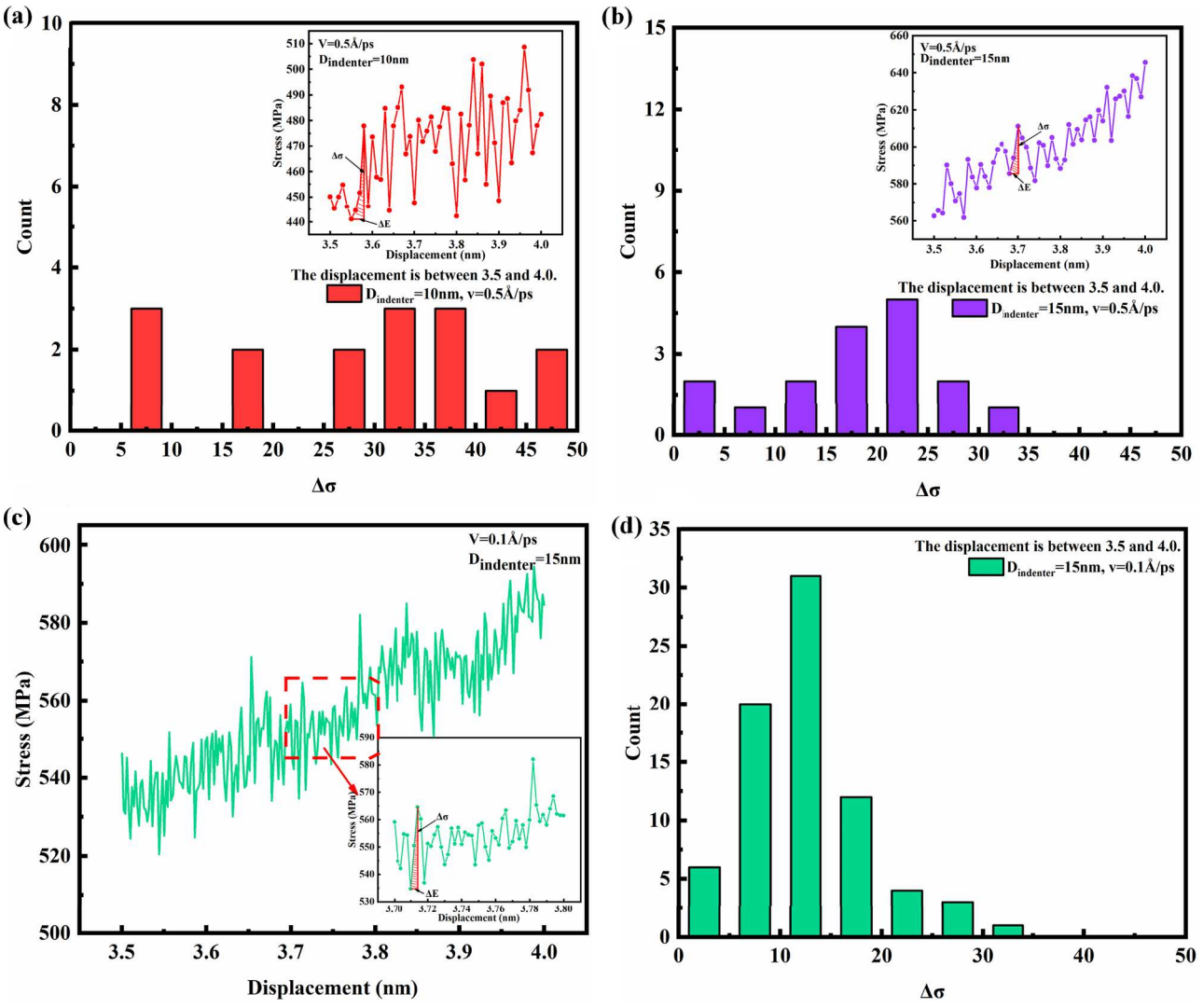

Fig. 16. Statistical charts of stress increment distribution for Cu50Zr50 amorphous alloy at different temperatures and strain rates for displacements from 3.5 to 4.0 nm. (a) $D_{indenter}$ = 10 nm, v = 0.5 Å/ps; (b) $D_{indenter}$ = 15 nm, v = 0.5 Å/ps; (c) $D_{indenter}$ = 15 nm, v = 0.1 Å/ps; (d) The statistical diagram of stress increment corresponding to Fig. 16(c).

both the intensity and quantity of shear strains. These observations can be attributed to the percolation effect, whereby the localized non-coordinated deformation induced by an increased volume fraction of the second phase leads to enhanced stress concentration at the interfaces between the amorphous and crystal phases. Consequently, this facilitates a substantial extension of shear bands [70]. Fig. 17(a) illustrates the tensile stress-strain curves of the amorphous composites with different sizes of the second phase. Both the amorphous alloys without a second phase and those with a diameter of 2 nm for the second phase exhibit distinctive avalanche behavior, characterized by a significant stress drop phenomenon. This avalanche phenomenon corresponds to the formation and propagation of the primary shear band. Conversely, nanograin diameters exceeding 3 nm do not display a sharp decrease in stress and can maintain a high level of strength. This trend can be attributed to the uniform distribution of strain across multiple shear bands, resulting in a more homogeneous deformation that effectively delays the inherent instability of the amorphous alloy. Additionally, the shear-strain cloud diagram reveals a tendency for necking. However, it should be noted that necking is not an inherent failure mechanism of amorphous alloys alone, and thus can be solely attributed to the presence of the nano-scale second phase.

To further investigate the influence of nanocrystals on shear bands, the present study examines the evolution of crystal structures, dislocation line lengths, and shear band morphology in soft copper crystals during the stretching process. Specifically, a second-phase material with a diameter of 4 nm is utilized as an example. Fig. 18(b) shows a decrease in dislocation line lengths with increasing macroscopic strain. The progression of dislocations, crystal structures, and shear bands in the center of the amorphous composites provides a clear illustration of the dislocation reduction process, as depicted in Fig. 19. Moreover, an analysis of the crystal structure using common neighbor analysis (CNA) reveals a significant increase in the formation of stacking faults, accompanied by a decrease in dislocations, as shown in Fig. 19(a) and (b). From these findings, we can summarize the reasons why nanoscale second phases impede shear band expansion without causing significant distortion as follows: (1). In the early stages of deformation, dislocations interact with numerous nano-scale stacking faults in the second phase, resulting in the formation of cut steps. Consequently, dislocation entanglement occurs, strengthening the second phase and impeding the extension of shear zones. Additionally, the interaction between dislocations and laminations contributes to this behavior, as illustrated in Fig. 19(c1) and (c2). (2). In the intermediate stage, although the number of dislocations decreases, more nano-scale stacking faults are formed. During this stage, the crystal phase is primarily strengthened by both

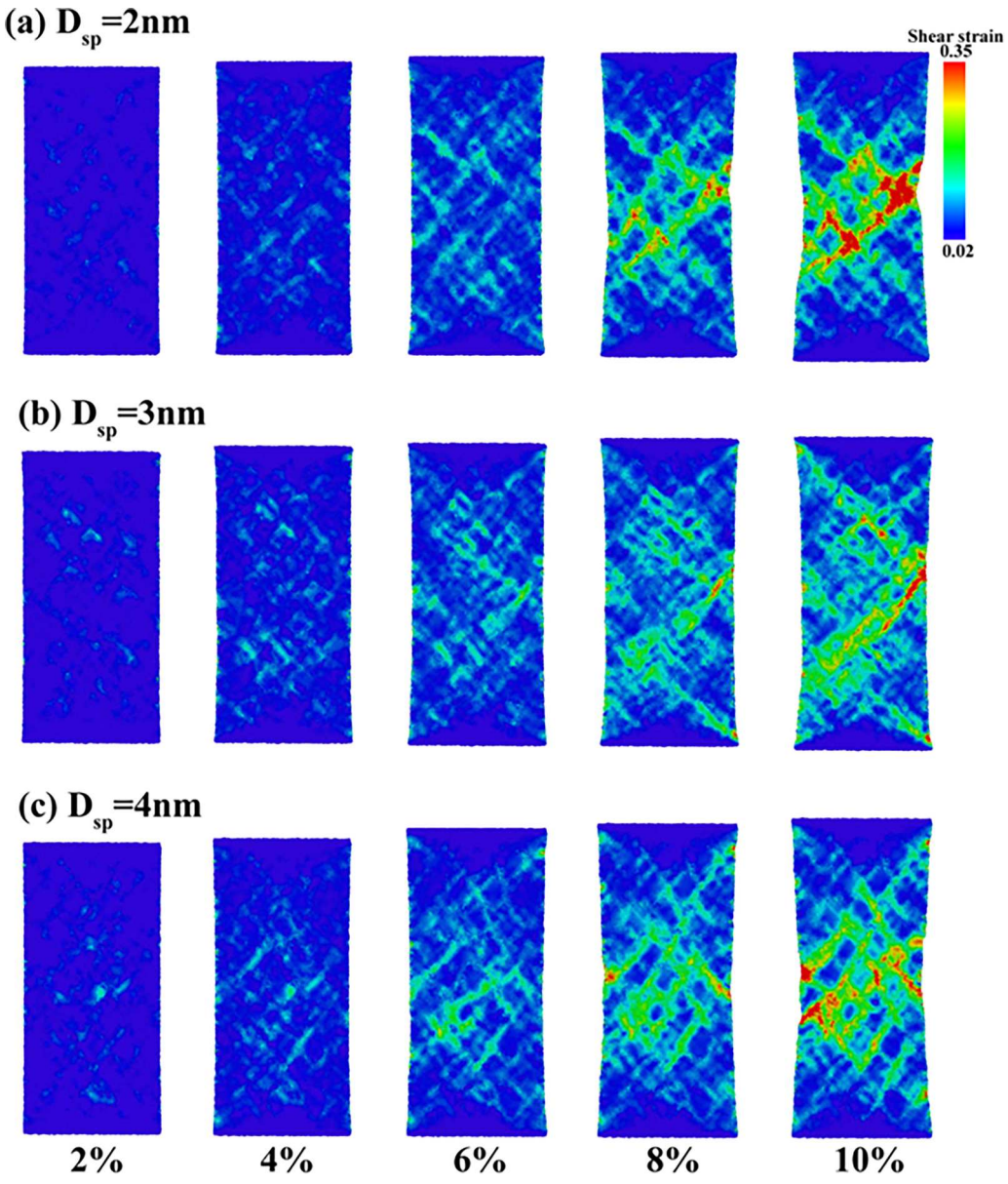

Fig. 17. Plot of shear strain distribution for CuZr-based amorphous composites containing nanoscale soft copper second phase. (a) D_{sp} = 2 nm; (b) D_{sp} = 3 nm; (c) D_{sp} = 4 nm.

dislocations and stacking faults. Fig. 19(c3) and (c4) demonstrate that stacking faults directly impede dislocation motion, creating a blocking mechanism. The presence of a stair-rod dislocation with a Burgers vector of 1/6<112> stabilizes the stacking fault and further reinforces the second-phase particles [71,72]. (3). In the final stage, the dislocation density is significantly reduced, and the nano-scale stacking faults serve as hard phases to strengthen the copper crystals, as depicted in Fig. 19 (c5). Fig. 19(d) illustrates that the synergistic strengthening mechanisms of nano-scale stacking faults and dislocations render the second phase with a 4 nm diameter less susceptible to shear band penetration. Instead, a shear-band cut-through mechanism, similar to that observed in micrometer-scale second phases, is observed [29]. Notably, the second phase with a 2 nm diameter is penetrated and severely deformed, underscoring the significant influence of volume fraction on the blocking effect of the second phase on shear bands, as shown in Fig. 20.

3.6. The relationship between intrinsic parameters and shear bands is in different models

In order to clarify the connection between microscopic mechanical behavior, shear band evolution and macroscopic mechanical performance, this section organizes the four models presented earlier and summarizes the impact of different influencing factors on the distribution of elastic energy density, normalized difference of strength, shear strain distribution, and sawtooth flow stress increment. The changes in these microscopic mechanical parameters can, in turn, affect the evolution behavior of shear bands as shown in Table 1. The extension modes of shear bands are mainly divided into single primary shear band extension and multiple shear band extension, where the primary shear band often brings about a reduction in plasticity. Therefore, in the table, shear bands are classified according to their extension trend, and for specific impacts of the extension degree of shear bands, please refer to the previous section. In addition, loading conditions, notch size, and nanoscale secondary phases can be regarded as external factors that could induce changes in the microscopic mechanical parameters,

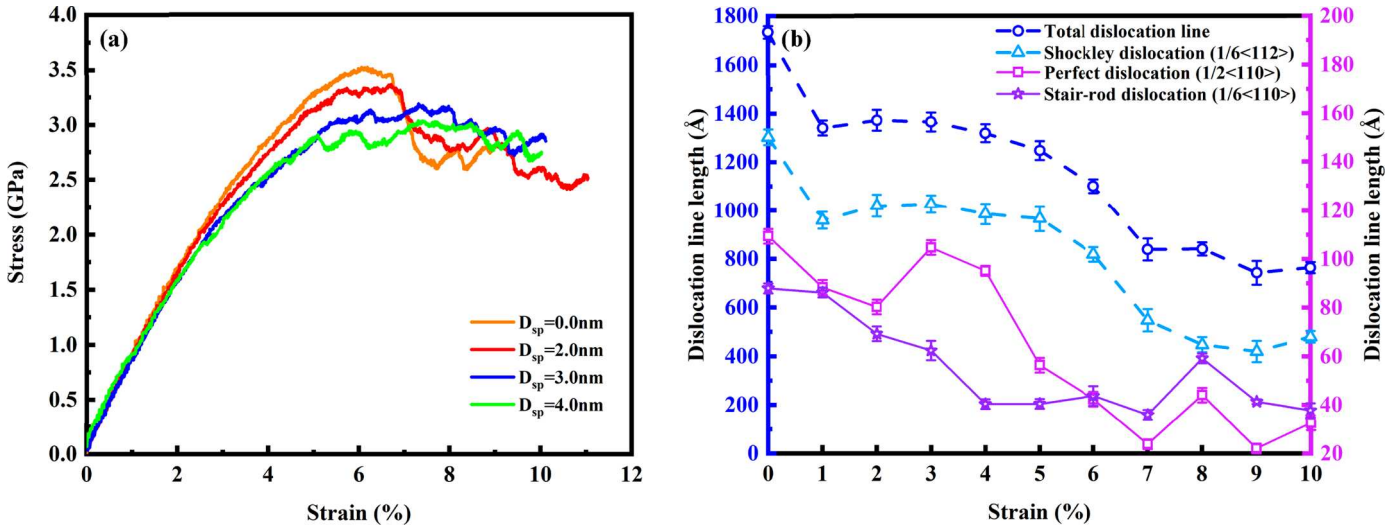

Fig. 18. (a) The tensile stress-strain curves of amorphous composites with different second phase sizes; (b) the evolution curve of the dislocation line length with increasing macroscopic strain at D_{sp} = 4 nm.

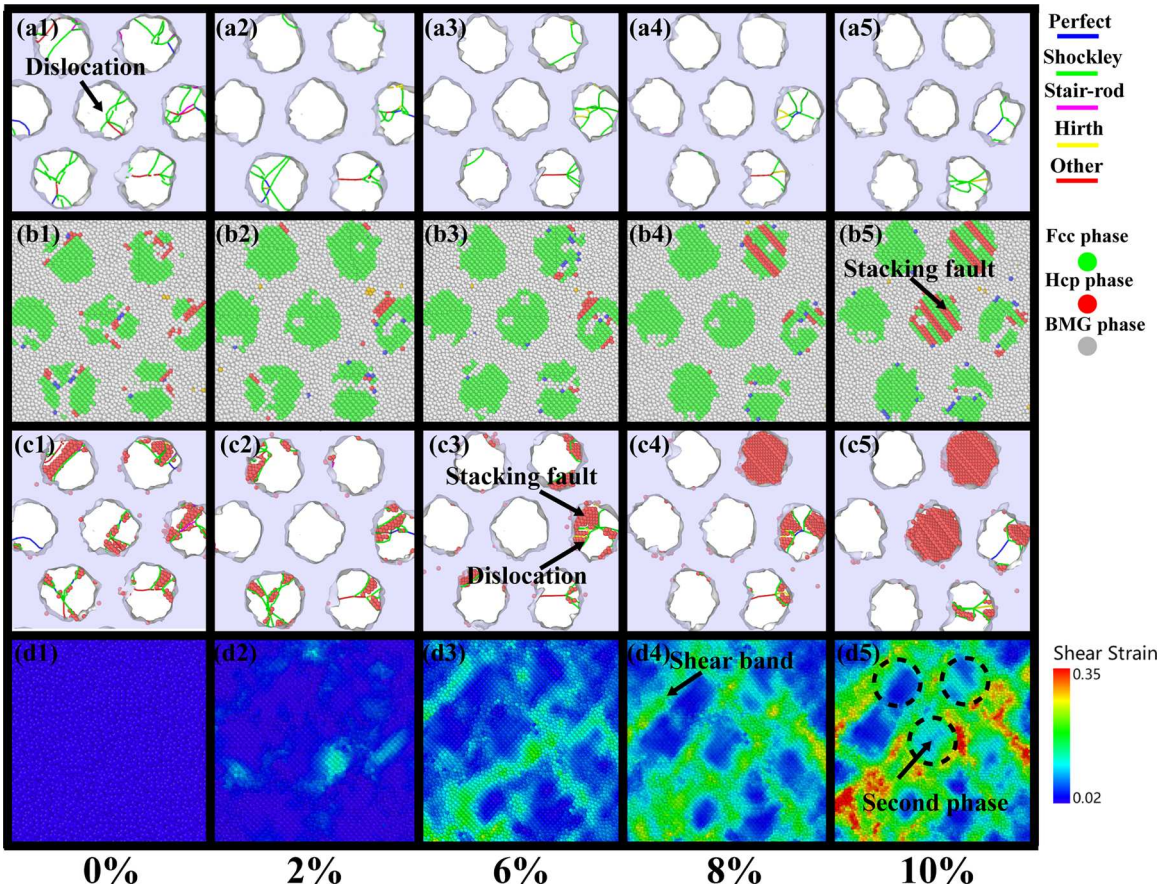

Fig. 19. Plots showing the evolution of dislocation lines (a1-a5), crystal structure (b1-b5), nano-stacking-fault distribution (c1-c5), and shear-strain fields (d1-d5) with increasing the macroscopic strain for amorphous composites where D_{sp} = 4 nm. Dislocation-configuration diagram, including Perfect dislocation (blue line), Shockley dislocation (green line), Stair-rod dislocation (purple line), Hirth dislocation (yellow line), and other dislocations (red line). Crystal-structure-configuration diagram with green atoms for an FCC structure, red for an hcp structure, and white for an amorphous structure. The red color in the shear-strain field represents the high-strain region.

ultimately affecting the evolution of shear bands. Firstly, for the complete amorphous model, temperature and loading rate affect the distribution of elastic energy density, leading to the emergence of chaotic and self-organized states. This ultimately influences the arrangement of shear bands, noting that the influence trend of temperature and loading rate on shear band distribution is opposite. Secondly, for the notch model, the size of the notch affects the stress drop value and the normalized difference of strength, reflecting the arrangement of shear

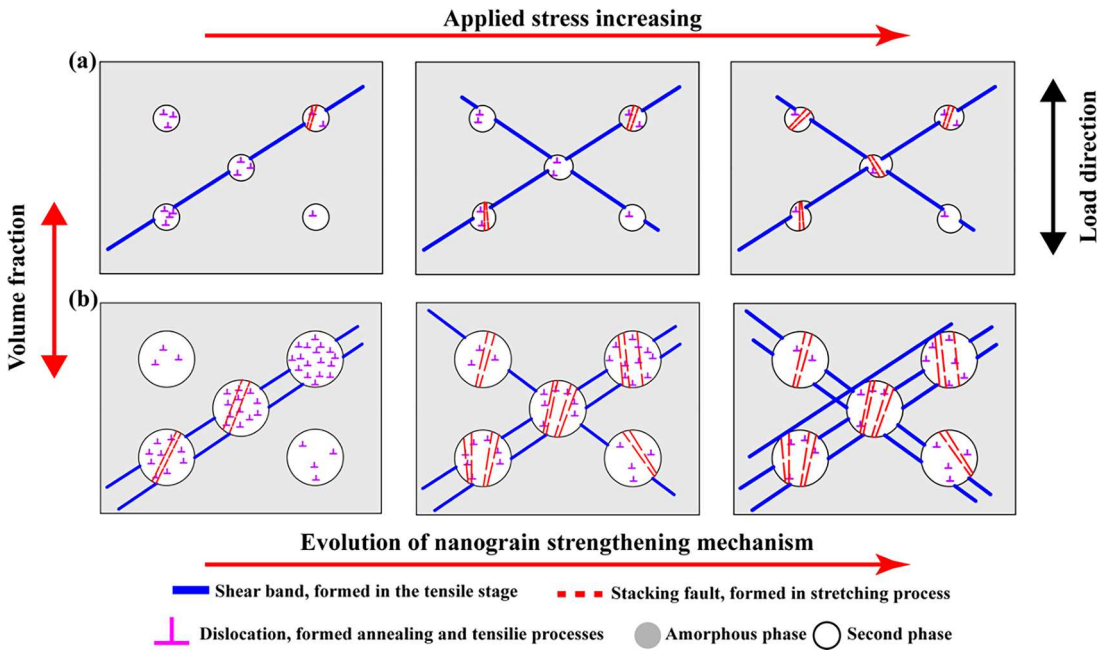

Fig. 20. Schematic illustration for the evolution of the reinforcement mechanisms in the nano-level second phase with increasing the loading strain, which is divided into three stages, the first-stage dislocation-dominated, the second-stage dislocation and stacking fault together, and the last stage nano-stacking-fault-dominated. (a) The lower volume fraction; and (b) The higher volume fraction.

bands. Furthermore, the distribution of shear strain can demonstrate the extent of shear band expansion, i.e., the higher the values of shear strain and the probability of high strain values, the easier it is to form a single dominant shear band. The serrated flow behavior of nanoindentation can effectively reflect the number of shear bands formed. The more sawtooth peaks, the greater the number of shear bands, and the larger the amplitude of the sawtooth, the greater the extent of shear band spreading. Finally, the increase in size of the second phase at the nanoscale can effectively reduce the value and concentration of shear strain, promote the formation of multiple shear bands, and enhance plasticity while reducing strength. This work establishes a connection between the micro-mechanical behavior, shear bands, and macro-mechanical properties, providing guidance for future design of amorphous alloys.

4. Conclusion

In this study, an amorphous-alloy model was established using molecular-dynamics simulations. The effects of temperature, loading rate, notch geometry, and second-phase size on shear-band evolution and mechanical properties were investigated, aiming to provide insights into the underlying mechanisms and guide the development of highly ductile and strong amorphous alloys.

(1) Analysis of the radial distribution function, bond-angle distribution, average atomic potential energy, and average atomic volume confirmed the successful formation of a CuZr-based amorphous alloy using an extremely cold method.
(2) The formation of shear bands was found to be highly sensitive to both temperature and strain rate during tensile loading. Higher temperatures and rates promoted the formation of multiple shear bands, leading to increased tensile plasticity. Conversely, lower temperatures exhibited more significant avalanche behavior. The relationship between the serrated rheological phenomenon and shear-band evolution was explained through analysis of stress-strain curves and calculation of the elastic-energy density distribution. Molecular-dynamics simulations supported the transition from plastic dynamics to self-organized critical behavior.
(3) The impact of notch geometry on tensile strength and plasticity was examined. The length of the notch had a more significant influence compared to the width. Increasing the notch length facilitated the formation and expansion of shear bands, resulting in a notable reduction in strength and plasticity. On the other hand, varying the notch width initially promoted the formation of a single shear band and subsequently facilitated the development of multiple shear bands.
(4) A comparative analysis was conducted to investigate the effects of different nanoindenter sizes and loading rates on shear-band evolution. Smaller indenters allowed for more extensive extension of shear bands, while lower loading rates activated a greater number of shear bands. Statistical analysis of serrated-flow behavior and stress-increment distribution provided insights into the micro-mechanical behavior, shear-band evolution, and macro-mechanical properties.
(5) The influence of second-phase size on shear-band hindrance at the nanoscale was explored. The presence of dislocations and nano-stacking faults in the nanocrystals strengthened the second phase, effectively impeding severe shear deformation. This finding highlights the synergistic strengthening mechanism and its role in preventing shear localization in the second phase.

CRediT authorship contribution statement

Huwen Ma: Conceptualization, Investigation, Methodology, Formal analysis, Writing – original draft, Validation. **Haizhuan Song:** Writing – review & editing. **Yuanfei Feng:** Supervision, Formal analysis, Investigation. **Zhi Lyu:** Writing – review & editing. **Li Feng:** Investigation, Formal analysis. **Tao Wen:** Conceptualization. **Wangchun Duan:** Investigation, Formal analysis. **Peter K. Liaw:** Resources, Conceptualization. **Yanchun Zhao:** Conceptualization, Investigation, Methodology, Formal analysis, Writing – original draft, Validation.

Declaration of Competing Interest

The authors declare that they have no known competing financial interests or personal relationships that could have appeared to influence

Table 1
The relationship between the parameters in different models.

Model	variable	Parameter	Shear band	Mechanical
Complete amorphous	Temperature increases	The elastic energy density shows a chaotic state.	Benefits multiple shear bands	Strength decreased
	Strain rate increase	The elastic energy density shows a self-organized critical state.	Benefits multiple shear bands	Strength increase
Notch amorphous	Notch length increase	The value of stress drops and normalized difference of strength decrease. Increased value and probability of shear strain.	Promotion a single main shear band	Reduced strength and plasticity
	Notch width increase	The value of stress drops and normalized difference of strength increase first and then decrease. The value and probability of shear strain decrease slightly.	Benefits multiple shear bands	Slightly affected
Nanoindentation Model	Indenter size decrease	The sawtooth flow density and amplitude increase.	Benefits multiple shear bands	
	Pressing rate increase	The sawtooth flow density increases, but the amplitude decreases.	Benefits multiple shear bands	
Composite material models	Second phase size increase	The shear strain value is reduced	Benefits multiple shear bands	The strength decreases and the plasticity increases.

the work reported in this paper.

Data availability

Data will be made available on request.

Acknowledgements

Yanchun Zhao gratefully acknowledges the fundings by Zhejiang Provincial Natural Science Foundation of China (Grant No. LY23E010002), National Natural Science Foundation of China (Grant No. 52061027), Science and Technology Program Project of Gansu Province (Grant No. 22YF7GA155, No. 22CX8GA109), Lanzhou Youth Science and Technology Talent Innovation Project(2023-QN-91). Huwen Ma, Li Feng and Yanchun Zhao acknowledges the support from Gansu Provincial Computing Center. Peter K. Liaw very much appreciates the support of the U.S. Army Research Office Project (W911NF-13-1-0438 and W911NF-19-2-0049) with the program managers, Drs. M. P. Bakas, S. N. Mathaudhu, and D. M. Stepp and the support from the National Science Foundation (DMR-1611180 and 1809640) with the program directors, Drs. J. Yang, G. Shiflet, and D. Farkas.

References

[1] C.A. Schuh, T.C. Hufnagel, U. Ramamurty, Mechanical behavior of amorphous alloys, Acta Mater. 55 (2007) 4067–4109, https://doi.org/10.1016/j.actamat.2007.01.052.
[2] W.H. Wang, Bulk metallic glasses with functional physical properties, Adv. Mater. 21 (2009) 4524–4544, https://doi.org/10.1002/adma.200901053.
[3] H.Y. Jung, S.J. Choi, K.G. Prashanth, M. Stoica, S. Scudino, S. Yi, U. Kühn, D. H. Kim, K.B. Kim, J. Eckert, Fabrication of Fe-based bulk metallic glass by selective laser melting: a parameter study, Mater. Des. 86 (2015) 703–708, https://doi.org/10.1016/j.matdes.2015.07.145.
[4] C. Cheng, X.M. Feng, Y.F. Shen, Microstructure and mechanical properties of Ti-Cu amorphous coating synthesized on pure Cu substrate by mechanical alloying method, Rare Met. 39 (2020) 1222–1228, https://doi.org/10.1007/s12598-018-1115-x.
[5] C. Zhang, R.Q. Guo, Y. Yang, Y. Wu, L. Liu, Influence of the size of spraying powders on the microstructure and corrosion resistance of Fe-based amorphous coating, Electrochim. Acta 56 (2011) 6380–6388, https://doi.org/10.1016/j.electacta.2011.05.020.
[6] A. Stukowski, Visualization and analysis of atomistic simulation data with OVITO–the open visualization tool, Model. Simul. Mater. Sci. 18 (2009), 015012, https://doi.org/10.1088/0965-0393/18/1/015012.
[7] M.P. Allen, D.J. Tildesley, Computer Simulation of Liquids, Oxford University Press, 2017, https://doi.org/10.1007/BF00646086.
[8] J.D. Honeycutt, H.C. Andersen, Molecular dynamics study of melting and freezing of small Lennard-Jones clusters, J. Phys. Chem. 91 (1987) 4950–4963, https://doi.org/10.1021/j100303a014.
[9] M.L. Falk, J.S. Langer, Dynamics of viscoplastic deformation in amorphous solids, Phys. Rev. E 57 (1998) 7192–7205, https://doi.org/10.1103/PhysRevE.57.7192.
[10] M. Sepúlveda-Macías, N. Amigo, G. Gutiérrez, Onset of plasticity and its relation to atomic structure in CuZr metallic glass nanowire: a molecular dynamics study, J. Alloys Compd. 655 (2016) 357–363, https://doi.org/10.1016/j.jallcom.2015.09.149.
[11] J. Jiang, W.F. Sun, N. Luo, Molecular dynamics study of microscopic deformation mechanism and tensile properties in AlxCoCrFeNi amorphous high-entropy alloys, Mater. Today Commun. 31 (2022) 103861–103869, https://doi.org/10.1016/j.mtcomm.2022.103861.
[12] G.J. Yang, B. Xu, C. Qi, L.T. Kong, J.F. Li, Effect of notch depth on the mechanical behavior of $Cu_{50}Zr_{50}$ metallic glasses revealed by molecular dynamics simulations, Intermetallics 93 (2018) 303–311, https://doi.org/10.1016/j.intermet.2017.10.010.
[13] D.P. Hua, W. Wang, D.W. Luo, Q. Zhou, S. Li, J.Q. Shi, M.S. Fu, H.F. Wang, Molecular dynamics simulation of the tribological performance of amorphous/amorphous nano-laminates, J. Mater. Sci. Technol. 105 (2022) 226–236, https://doi.org/10.1016/j.jmst.2021.07.027.
[14] H.Y. Song, M. Wang, Q. Deng, Y.L. Li, Deformation mode transitions in Cu50Zr50 amorphous/Cu crystalline nanomultilayer: a molecular dynamics study, J. Non-Cryst. Solids 490 (2018) 13–21, https://doi.org/10.1016/j.jnoncrysol.2018.03.036.
[15] P. Sun, C.X. Peng, Y. Cheng, G. Zhang, P.F. Wang, L.J. Jia, L. Wang, Mechanical behavior of CuZr dual-phase nanocrystal-metallic glass composites, Comput. Mater. Sci. 163 (2019) 290–300, https://doi.org/10.1016/j.commatsci.2019.03.046.
[16] N. Amigo, M. Sepulveda-Macias, G. Gutierrez, Enhancement of mechanical properties of metallic glass nanolaminates via martensitic transformation: atomistic deformation mechanism, Mater. Chem. Phys. 225 (2019) 59–168, https://doi.org/10.1016/j.matchemphys.2018.12.050.
[17] W.W. Li, H.Y. Song, J.L. Dai, J.Y. Wang, M.R. An, Y.L. Li, Effect of shape memory alloys on the mechanical properties of metallic glasses: a molecular dynamics study, Comput. Mater. Sci. 187 (2021) 110088–110094, https://doi.org/10.1016/j.commatsci.2020.110088.
[18] M. Sepulveda-Macias, N. Amigo, G. Gutierrez, Tensile behavior of Cu50Zr50 metallic glass nanowire with a B2 crystalline precipitate, Physica B 531 (2018) 64–69, https://doi.org/10.1016/j.physb.2017.12.005.
[19] X.Y. Wang, S.D. Feng, L. Qi, W. Gao, S.L. Zhang, Mechanical properties of $Cu_{50}Zr_{50}$ amorphous/B2-CuZr crystalline composites studied by molecular dynamic method, J. Non-Cryst. Solids 568 (2021) 120942–120947, https://doi.org/10.1016/j.jnoncrysol.2021.120942.

[20] P.H. Cao, K.A. Dahmen, A. Kushima, W.J. Wright, H.S. Park, M.P. Short, S. Yip, Nanomechanics of slip avalanches in amorphous plasticity, J. Mech. Phys. Solids 114 (2018) 158–171, https://doi.org/10.1016/j.jmps.2018.02.012.

[21] K.S. Zhu, P.J. Tao, C.H. Zhang, Z.H. Zhao, W.J. Zhang, Y.Z. Yang, K. Kaviyarasu, Effect of strain rates on the plastic deformation behavior and serrated flow of $Zr_{55.7}Cu_{22.4}Ni_{7.2}Al1_{4.7}$ bulk metallic glass, Mater. Today Commun. 27 (2021) 102320–102326, https://doi.org/10.1016/j.mtcomm.2021.102320.

[22] G.K. Liao, Z.L. Long, M.S.Z. Zhao, M. Zhong, W. Liu, W. Chai, Serrated flow behavior in a Pd-based bulk metallic glass under nanoindentation, J. Non-Cryst. Solids 460 (2017) 47–53, https://doi.org/10.1016/j.jnoncrysol.2017.01.010.

[23] W.H. Jiang, F. Jiang, B.A. Green, F.X. Liu, P.K. Liaw, Electrochemical corrosion behavior of a Zr-based bulk-metallic glass, Appl. Phys. Lett. 91 (2007) 041904–041906, https://doi.org/10.1063/1.2762282.

[24] F.H.D. Torre, D. Klaumünzer, R. Maaß, J.F. Löffler, Stick-slip behavior of serrated flow during inhomogeneous deformation of bulk metallic glasses, Acta Mater. 58 (2010) 3742–3750, https://doi.org/10.1016/j.actamat.2010.03.011.

[25] T. Richeton, J. Weiss, F. Louchet, Breakdown of avalanche critical behaviour in polycrystalline plasticity, Nat. Mater. 4 (2005) 465–469, https://doi.org/10.1038/nmat1393.

[26] P. Bak, C. Tang, Earthquakes as a self-organized critical phenomenon, J. Geophys. Res. Solid Earth 94 (1989) 15635–15637, https://doi.org/10.1029/JB094iB11p15635.

[27] M.S. Bharathi, M. Lebyodkin, G. Ananthakrishna, C. Fressengeas, L.P. Kubin, Multifractal burst in the spatiotemporal dynamics of jerky flow, Phys. Rev. Lett. 87 (2001) 165508–165511, https://doi.org/10.1103/PhysRevLett.87.165508.

[28] X. Wang, W. Zhang, Y.C. Zhao, H.B. Bei, Y.F. Gao, Micromechanical investigation of the role of percolation on ductility enhancement in metallic glass composites, Mater. Sci. Eng, A 769 (2020) 138531–138541, https://doi.org/10.1016/j.msea.2019.138531.

[29] Z.Q. Liu, R. Li, G. Liu, W.H. Su, H. Wang, Y. Li, M.J. Shi, X.K. Luo, G.J. Wu, T. Zhang, Microstructural tailoring and improvement of mechanical properties in CuZr-based bulk metallic glass composites, Acta Mater. 60 (2012) 3128–3139, https://doi.org/10.1016/j.actamat.2012.02.017.

[30] H.W. Ma, Y.C. Zhao, X. Wang, D. Ma, Y.F. Gao, Synergistic effects of microstructural inhomogeneity and phase-transformation-induced plasticity for ductility improvements in metallic glass composites, Mater. Sci. Eng. A 849 (2022) 143491–143504, https://doi.org/10.1016/j.msea.2022.143491.

[31] K.S. Ming, Z.W. Zhu, W.Q. Zhu, B. Feng, B.Q. Wei, P.K. Liaw, X.D. Wei, J. Wang, S. J. Zheng, Enhancing strength and ductility via crystalline-amorphous nanoarchitectures in TiZr-based alloys, Sci. Adv. 8 (2022) 2884, https://doi.org/10.1126/sciadv.abm2884.

[32] G. Wu, K.C. Chang, L.L. Zhu, L.G. Sun, J. Lu, Dual-phase nanostructuring as a route to high-strength magnesium alloys, Nature 545 (2017) 80–83, https://doi.org/10.1038/nature21691.

[33] S. Plimpton, Fast parallel algorithms for short-range molecular dynamics, J. Comput. Phys. 117 (1995) 1–19, https://doi.org/10.1006/jcph.1995.1039.

[34] C.Y. Cheng, Y.Y. Guo, Y.M. Zou, A.J. Ong, A.L.Y. Tok, S.Z. Li, Melting mechanisms of Pt-based multimetallic spherical nanoparticles by molecular dynamics simulation, Rare Met. 42 (2023) 406–417, https://doi.org/10.1007/s12598-022-02160-5.

[35] Y. Wang, H.F. Zhan, C. Yang, Y. Xiang, Y.Y. Zhang, Formation of carbon nanoscrolls from graphene nanoribbons: a molecular dynamics study, Comput. Mater. Sci. 96 (2015) 300–305, https://doi.org/10.1016/j.commatsci.2014.09.039.

[36] Z.D. Sha, P.S. Branicio, H.P. Lee, T.E. Tay, Strong and ductile nanolaminate composites combining metallic glasses and nanoglasses, Int. J. Plast. 90 (2017) 231–241, https://doi.org/10.1016/j.ijplas. 2017.01.010.

[37] A. Stukowski, Visualization and analysis of atomistic simulation data with OVITO-the open visualization tool, Model. Simul. Mater. Sci. 18 (2010) 2154–2162, https://doi.org/10.1088/0965-0393/18/1/015012.

[38] D.P. Hua, W.T. Ye, Q. Jia, Q. Zhou, Q.S. Xia, J.Q. Shi, Y.Y. Deng, H.F. Wang, Molecular dynamics simulation of nanoindentation on amorphous/amorphous nanolaminates, Appl. Surf. Sci. 511 (2020), 145545, https://doi.org/10.1016/j.apsusc.2020.145545.

[39] M.I. Mendelev, D.J. Sordelet, M.J. Kramer, Using atomistic computer simulations to analyze x-ray diffraction data from metallic glasses, J. Appl. Phys. 102 (2007), https://doi.org/10.1063/1.2769157.

[40] B.A. Sun, W.H. Wang, The fracture of bulk metallic glasses, Prog. Mater. Sci. 74 (2015) 211–307, https://doi.org/10.1016/j.pmatsci.2015.05.002.

[41] Y. Hiraoka, T. Nakamura, A. Hirata, Y. Nishiura, Hierarchical structures of amorphous solids characterized by persistent homology, PNAS 113 (2016) 7035–7040, https://doi.org/10.1073/pnas.1520877113.

[42] H.L. Peng, M.Z. Li, W.H. Wang, Structural signature of plastic deformation in metallic glasses, Phys. Rev. Lett. 106 (2011), 135503, https://doi.org/10.1103/PhysRevLett.106.135503.

[43] H.L. Peng, M.Z. Li, W.H. Wang, C.Z. Wang, K.M. Ho, Effect of local structures and atomic packing on glass forming ability in Cu_xZr_{100-x} metallic glasses, Appl. Phys. Lett. 96 (2010), 021901, https://doi.org/10.1063/1.3282800.

[44] M.I. Mendelev, M.J. Kramer, R.T. Ott, D.J. Sordelet, D. Yagodin, P. Popel, Development of suitable interatomic potentials for simulation of liquid and amorphous Cu-Zr alloys, Philos. Mag. 89 (2009) 967–987, https://doi.org/10.1080/14786430902832773.

[45] V.K. Sutrakar, D.R. Mahapatra, Stress-induced martensitic phase transformation in Cu-Zr nanowires, Mater. Lett. 63 (2009) 1289–1292, https://doi.org/10.1016/j.matlet.2009.02.064.

[46] K.N. Lad, N. Jakse, A. Pasturel, How closely do many-body potentials describe the structure and dynamics of Cu-Zr glass-forming alloy? J. Chem. Phys. 146 (2017), 124502 https://doi.org/10.1063/1.4979125.

[47] F. Li, X.J. Liu, H.Y. Hou, G. Chen, G.L. Chen, Structural origin underlying poor glass forming ability of Al metallic glass, J. Appl. Phys. 110 (2011) 013519–013525, https://doi.org/10.1063/1. 3605510.

[48] X.X. Yue, C.T. Liu, S.Y. Pan, A. Inoue, P.K. Liaw, C. Fan, Effect of cooling rate on structures and mechanical behavior of Cu50Zr50 metallic glass: a molecular-dynamics study, Physica B 547 (2018) 48–54, https://doi.org/10.1016/j.physb.2018.07.030.

[49] M.X. Li, Y.T. Sun, C. Wang, L.W. Hu, S. Sohn, J. Schroers, W.H. Wang, Y.H. Liu, Data-driven discovery of a universal indicator for metallic glass forming ability, Nat. Mater. 21 (2022) 165–172, https://doi.org/10.1038/s41563-021-01129-6.

[50] Y.Q. Cheng, E. Ma, Atomic-level structure and structure–property relationship in metallic glasses, Prog. Mater. Sci. 56 (2011) 379–473, https://doi.org/10.1016/j.pmatsci.2010.12.002.

[51] Q.K. Li, M. Li, Molecular dynamics simulation of intrinsic and extrinsic mechanical properties of amorphous metals, Intermetallics 14 (2006) 1005–1010, https://doi.org/10.1016/j.intermet.2006.01.019.

[52] A.S. Argon, Plastic deformation in metallic glasses, Acta Metall. 27 (1979) 47–58, https://doi.org/10.1016/0001-6160(79)90055-5.

[53] G.M. Luo, J.S. Wu, J.F. Fan, H.S. Shi, Y.J. Lin, J.G. Zhang, Deformation behavior of an ultrahigh carbon steel (UHCS-3.0 Si) at elevated temperature, Mater. Sci. Eng. A 379 (2004) 302–307, https://doi.org/10.1016/j.msea.2004.02.056.

[54] H.B. Yu, J. Hu, X.X. Xia, B.A. Sun, X.X. Li, W.H. Wang, H.Y. Bai, Stress-induced structural inhomogeneity and plasticity of bulk metallic glasses, Scr. Mater. 61 (2009) 640–643, https://doi.org/10.1016/j.scriptamat.2009.06.005.

[55] Y. Song, X. Xie, J.J. Luo, P.K. Liaw, H.R. Qi, Y.F. Gao, Seeing the unseen: uncover the bulk heterogeneous deformation processes in metallic glasses through surface temperature decoding, Mater. Today 20 (2017) 9–15, https://doi.org/10.1016/j.mattod.2016.12.002.

[56] A. Wolf, J.B. Swift, H.L. Swinney, J.A. Vastano, Determining Lyapunov exponents from a time series, Physica D 16 (1985) 285–317, https://doi.org/10.1016/0167-2789(85)90011-9.

[57] H. Li, C. Fan, K.X. Tao, H. Choo, P.K. Liaw, Compressive behavior of a Zr-Based metallic glass at cryogenic temperatures, Adv. Mater. 18 (2006) 752–754, https://doi.org/10.1002/adma.200501990.

[58] G.H. Majzoobi, J. Nemati, The effect of notch geometry on tensile strength at low and intermediate strain rates, Strain 47 (2011) 326–336, https://doi.org/10.1111/j.1475-1305.2009.00693.x.

[59] X.D. Yuan, Z.Q. Zhang, Q.W. Gao, L. Zhou, K.K. Song, X.Y. Zou, D. Dopu, L.N. Hu, B.A. Sun, J. Eckert, Enhanced mechanical properties of Zr65Cu15Ni10Al10 bulk metallic glass by simultaneously introducing surface grooves and multiple shear bands, J. Mater. Res. Technol. 21 (2022) 1490–1506, https://doi.org/10.1016/j.jmrt.2022.09.117.

[60] Y.Q. Cheng, A.J. Cao, W.H. Sheng, E. Ma, Local order influences initiation of plastic flow in metallic glass: effects of alloy composition and sample cooling history, Acta Mater. 56 (2008) 5263–5275, https://doi.org/10.1016/j.actamat.2008.07.011.

[61] H.K. Kim, M. Lee, K.R. Lee, J.C. Lee, How can a minor element added to a binary amorphous alloy simultaneously improve the plasticity and glass-forming ability? Acta Mater. 61 (2013) 6597–6608, https://doi.org/10.1016/j.actamat.2013.07.044.

[62] R.T. Hill, On discontinuous plastic states, with special reference to localized necking in thin sheets, J. Mech. Phys. Solids 1 (1952) 19–130, https://doi.org/10.1016/0022-5096(52)90003-3.

[63] X.X. Yue, J. Brechtl, F.J. Wang, Z.X. Chang, P.K. Liaw, C. Fan, Deformation behavior of annealed Cu64Zr36 metallic glass via molecular dynamics simulations, Mater. Des. 191 (2020) 108660–108669, https://doi.org/10.1016/j.matdes.2020.108660.

[64] M.W. Chen, A. Inoue, W. Zhang, T. Sakurai, Extraordinary plasticity of ductile bulk metallic glasses, Phys. Rev. Lett. 96 (2016) 245502–245505, https://doi.org/10.1103/PhysRevLett.96.245502.

[65] L.L. Wang, Z. Wang, L.N. Hu, Rejuvenation to relaxation transition and liquid memory effect in La-based metallic glasses with different energy states, Intermetallics 156 (2023), 107864, https://doi.org/10.1016/j.intermet.2023.107864.

[66] W.H. Jiang, M. Atzmon, Rate dependence of serrated flow in a metallic glass, J. Mater. Res. 18 (2003) 755–757, https://doi.org/10.1016/S1359-6454(02)00303-8.

[67] H. Huang, H.W. Zhao, Indenter geometry affecting indentation behaviors of the Zr-based bulk metallic glass, Mater. Trans. 55 (2014) 1400–1404, https://doi.org/10.2320/matertrans.M2014136.

[68] R. Maaß, D. Klaumünzer, J.F. Löffler, Propagation dynamics of individual shear bands during inhomogeneous flow in a Zr-based bulk metallic glass, Acta Mater. 59 (2011) 3205–3213, https://doi.org/10.1016/j.actamat.2011.01.060.

[69] A. Inoue, C. Fan, J. Saida, T. Zhang, High-strength Zr-based bulk amorphous alloys containing nanocrystalline and nanoquasicrystalline particles, Sci. Technol. Adv. Mater. 1 (2000) 73–86, https://doi.org/10.1016/S1468-6996(00)00009-7.

[70] Z.Q. Liu, G. Liu, R.T. Qu, Z.F. Zhang, S.J. Wu, T. Zhang, Microstructural percolation assisted breakthrough of trade-off between strength and ductility in CuZr-based

metallic glass composites, Sci. Rep. 4 (2014) 4167–4172, https://doi.org/10.1038/srep04167.
[71] R.G. Liu, J. Tang, J.X. Jiang, X.Y. Li, Y.J. Wei, Stacking fault induced hardening and grain size effect in nanocrystalline CoNiCrFeMn high-entropy alloy, Extrem. Mech. Lett. 56 (2022) 101875–101880, https://doi.org/10.1016/j.eml.2022.101875.
[72] Q.S. Pan, L.X. Zhang, R. Feng, Q.H. Lu, K. An, A.C. Chuang, J.D. Poplawsky, P. K. Liaw, Gradient cell-structured high-entropy alloy with exceptional strength and ductility, Science 374 (2021) 984–989, https://doi.org/10.1126/science.abj8114.